J. Fluid Mech. (1997), *vol.* 330, *pp.* 271–305

An experimental study of compressible turbulent mixing enhancement in swirling jets

By JONATHAN W. NAUGHTON†, LOUIS N. CATTAFESTA III‡ AND GARY S. SETTLES

Department of Mechanical Engineering, The Pennsylvania State University, University Park, PA 16802, USA

(Received 14 June 1994 and in revised form 22 July 1996)

Compressible jets with various amounts of swirl and compressibility are investigated experimentally. The mixing-layer growth rate is obtained from time-averaged images of the mixing layer using the planar laser scattering (PLS) technique, and the swirl is quantified with laser Doppler velocimetry and intrusive probes. The results conclusively demonstrate that the addition of swirl to the jet increases entrainment by up to 60% compared to a corresponding non-swirling case. Instantaneous PLS images reveal modified turbulent structure in the mixing layer of the swirling-jet cases. In particular, analysis of these images indicates that both the spatial extent and amplitude of the largest turbulent fluctuations are increased when swirl is added. Based upon these results, a parameter β that correlates the observed growth-rate enhancement is proposed. This parameter is derived assuming that the streamwise vorticity, generated in the mixing layer by the addition of small amounts of swirl, causes additional turbulent mixing that increases the growth rate. When the available growth-rate data for swirling jets are plotted against this parameter, they collapse to a single curve with increased enhancement for higher values of β. This result implies that the degree of enhancement actually increases with compressibility, although the dimensional growth rates for the present compressible swirling-jet cases are still less than those of their incompressible counterparts.

1. Introduction

The enhancement of the growth rates of compressible turbulent mixing layers has received a great amount of attention in the past decade due to the renewed interest in supersonic combustion. During this period, several studies were initiated to investigate the nature of these mixing layers, and specifically to address the reduced mixing-layer growth rates observed (as compared to the incompressible case). Although these studies have resulted in a better understanding of the physical processes occurring in such mixing layers, all attempts to significantly enhance mixing-layer growth and entrainment have met with little success. Interest in this area of research continues, with applications such as jet noise and jet-plume growth further fuelling the desire to acquire an understanding of compressible turbulent mixing layers. Note that the term 'mixing', which normally applies to processes at the molecular level, is used throughout this paper when referring to entrainment and growth of the mixing layer.

† Present address: MCAT, Inc., Mountain View, CA 94043, USA.
‡ Present address: High Technology Corporation, Hampton, VA 23666, USA.

In this paper, the results of an experimental study of mixing enhancement in which varying levels of swirl were added to axisymmetric jets with different degrees of compressibility are discussed. These results conclusively demonstrate that the mixing-layer growth rates of the swirling jets are greater than those of their non-swirling counterparts when all other quantities are held constant. The swirl-induced mixing enhancement is then linked to a modification of the turbulence in the mixing layers surrounding the swirling jets. Next, the success of this enhancement technique is discussed and compared with other related studies. Finally, a parameter that correlates the enhanced mixing-layer growth rates of swirling jets is presented.

Although the results of other mixing-layer studies are too vast to review thoroughly here, their highlights are summarized below. For a more comprehensive overview, the interested reader is referred to the survey by Dimotakis (1991). Early theories pointed to the large density ratios existing between the two component streams as the cause of the decreased mixing rates observed in compressible turbulent mixing layers. However, Brown & Roshko (1974) were able to show that this reduced mixing could not be attributed solely to density ratio, but rather was due, in part, to compressibility. Following the work of Bogdanoff (1983), Papamoschou & Roshko (1988) determined that the key parameter governing the effect of compressibility on turbulent mixing was the convective Mach number, the Mach number at which the structures in the shear layer are presumed to move with respect to the two component streams. These compressibility parameters are defined as

$$M_{c,1} = (u_1 - u_c)/a_1 \tag{1.1a}$$

and

$$M_{c,2} = (u_c - u_2)/a_2, \tag{1.1b}$$

where u is the velocity, M is the Mach number, a is the acoustic velocity, subscript c refers to 'convective', and the subscripts 1 and 2 refer to the high-speed (primary) and low-speed (secondary) streams, respectively. Coles (1985) suggested that, in a coordinate system travelling at the convective velocity, a stagnation point should exist between turbulent structures. Papamoschou & Roshko (1988) used this idea to show that the convective velocity u_c in (1.1a) and (1.1b) was given by

$$u_c = u_1(1 + RS^{1/2})/(1 + S^{1/2}), \tag{1.2}$$

where R is the velocity ratio (u_2/u_1), and S is the density ratio (ρ_2/ρ_1). When they non-dimensionalized their experimentally determined growth rates by the incompressible value, which was calculated using identical values of R and S, and plotted the result against the convective Mach number, the data collapsed to reveal a significant reduction in mixing due to compressibility.

In response to these results, several studies were initiated to investigate compressible turbulent mixing layers further. Laser Doppler velocimetry (LDV) measurements (Elliot & Samimy 1990; Goebel & Dutton 1991) determined that these mixing layers extracted less energy from the mean flow than their incompressible counterparts, as revealed by reduced turbulence levels and diminished growth rates. Furthermore, flow visualization studies (Clemens & Mungal 1992; Fourgette, Mungal & Dibble 1991) identified that a modification of turbulent structures accompanied these phenomena. Specifically, a transition from organized spanwise-oriented two-dimensional to highly irregular three-dimensional structures was observed as compressibility increased. In accordance with these observations, linear stability analyses of mixing layers (Sandham & Reynolds 1990; Jackson & Grosch 1989; Morris, Giridharan

& Lilley 1990) revealed a decrease in amplification rate and an increase in the importance of three-dimensional instabilities with increasing compressibility. Further indications of structure modification were evident in direct numerical simulation studies of compressible mixing layers (Sandham & Reynolds 1990; Lele 1989). In these low-Reynolds number simulations, swept flattened vortical structures and decreased growth rates were observed. These results were attributed to a redistribution of vorticity brought about by changes in the baroclinic and dilatation terms in the vorticity equation. A more complete summary of compressibility effects on turbulence is given by Lele (1994).

Although the above discoveries were illuminating, they failed to provide a physical mechanism responsible for the reduced mixing rates observed. One possible mechanism is that communication between two-dimensional structures oriented perpendicular to the primary flow direction is increasingly restricted as the Mach number increases (Papamoschou 1990). This reduced communication inhibits the initial roll-up and eventual pairing of spanwise (planar) or azimuthal (axisymmetric) vortical structures, thereby producing weak elongated vortices (Morkovin 1992). These vortical structures are no longer able to entrain as much fluid from outside the mixing layer and are thus less efficient at extracting energy from the mean flow for mixing. As a result, there is less energy to transfer to the smaller streamwise vortical structures through vortex stretching, and thus the turbulence energy at all scales is reduced.

In contrast to spanwise or axisymmetric structures, streamwise vortical structures are not subject to communication problems since they primarily interact in the spanwise direction (Morkovin 1992). Therefore, these structures should continue to enlarge, entrain fluid, and extract energy from the mean flow even under highly compressible conditions. Some authors (e.g. Papamoschou & Roshko 1988) have suggested that naturally occurring three-dimensional structures (which have streamwise components) cause the turbulent mixing layer growth rate to asymptote to a value that is roughly 20% of the corresponding incompressible value. Assuming that this suggestion is valid, the addition of three-dimensionality at any significant level of compressibility should have beneficial effects on mixing. Just as a swept wing postpones the effects of wave drag to higher Mach numbers, these swept (in planar mixing layers) or helical (in axisymmetric mixing layers) structures might reduce the adverse effect of compressibility on growth rate. One method of creating a streamwise component of vorticity is the addition of a tangential-velocity component (u_θ) to an axisymmetric jet. This means of adding three-dimensionality is investigated in this study.

The concept of swirl-enhanced mixing is not new. Based on observations of low-speed and transonic swirling flows, Swithenbank & Chigier (1969) suggested that the phenomenon responsible for increased mixing in these flows might cause similar results in compressible flows as well. In response to this suggestion, Povinelli & Ehlers (1972) and Schetz & Swanson (1973) investigated swirling jets injected into a supersonic co-flowing stream. From results obtained with intrusive probes, both studies concluded that the addition of swirl did little to enhance the mixing. However, neither study established the amount of swirl added to the flow, and thus their results were not conclusive for swirling jets in general.

In contrast to these early results, more recent studies have indicated that swirl does substantially enhance compressible turbulent mixing. Cutler, Levey & Kraus (1993) performed extensive flow-field measurements in a Mach 2.2 swirling free jet. The growth rates of the turbulent mixing layers surrounding this jet flow with different levels of swirl were evaluated using planar laser scattering (PLS). Their results revealed

that the growth rates increased with the degree of swirl and were up to three times higher than that of the non-swirling jet for the cases studied.

Another recent study involved a linear stability analysis of a weakly swirling compressible jet (Khorrami 1995). It was found that swirl de-stabilized otherwise stable negative-helical modes of the jet. Compressibility damped the amplification rate of these modes, but they were less damped than in the non-swirling case. Although this study did not directly address the mixing layer surrounding the jet, the results clearly indicate that additional instabilities are supported in swirling jets.

Although some evidence exists that supports the view that swirl enhances mixing, several questions remain unanswered: Why do the conclusions of the previous studies disagree? What are the mechanisms causing swirl-enhanced mixing? How does swirl enhancement (if it exists) depend upon compressibility and the amount of swirl? How much enhancement can reasonably be expected? The present study was designed to address these questions. It differs from its predecessors in that it quantifies swirl and mixing-layer growth rates over a range of swirl strength and compressibility. Furthermore, to the best of our knowledge, the turbulent structure of swirling compressible mixing layers is investigated for the first time in this study.

The remainder of the article is organized as follows. The experimental hardware and instrumentation are described in §2 and §3, respectively. The test cases for the current study are given in §4, and the swirling-jet flow-field surveys, mixing-layer growth rate measurements, and turbulent structure visualization results are presented in §5, §6, and §7, respectively. In §8, the results are discussed, and, in §9, a parameter that correlates the enhanced mixing-layer growth due to swirl is proposed. Some conclusions are offered in §10.

2. Experimental hardware

The mixing-layer growth rate experiments were performed in the Penn State University Supersonic Wind Tunnel (PSUSWT). This facility provided the supersonic co-flowing air stream into which the primary swirling flow was injected. The tunnel is of the intermittent blow-down type with a Mach number range of 1.5 to 4.0. The pressure reservoir has a volume of 57 m^3 and can provide total pressures of up to 2 MPa. The total pressure (P_0) of the facility is regulated by a microprocessor-controlled valve. Typical test times for the current tests at $P_0 = 1.5$ MPa, $M = 4.0$, were 30 s with corresponding Reynolds numbers of $68 \times 10^6\ m^{-1}$. This facility is also equipped with a gas injection system that supplies an alternative regulated high-pressure gas source. This system uses either gas cylinders or the wind-tunnel pressure reservoir as its source.

To quantify the swirl of the test cases a different facility was used. The Penn State University Free Jet Facility (PSUFJF) was chosen since it provided additional optical access necessary for some of the experimental techniques used. The same gas sources as those used for the wind-tunnel injection system were employed. In this facility, the pressure-regulated gas flows into a stilling chamber and then enters one of several interchangeable supersonic nozzles. Seeding of this flow for LDV and flow visualization is accomplished by means of a TSI atomizing seeder located inside a pressure reservoir connected to the stilling chamber. This seeder introduces sub-micron silicon oil droplets into the stilling chamber thus allowing them to mix with the flow before entering the nozzle.

In order to produce a variable-strength swirling primary flow in the test section of the PSUSWT, a vortex injector was designed. The injector, shown mounted in

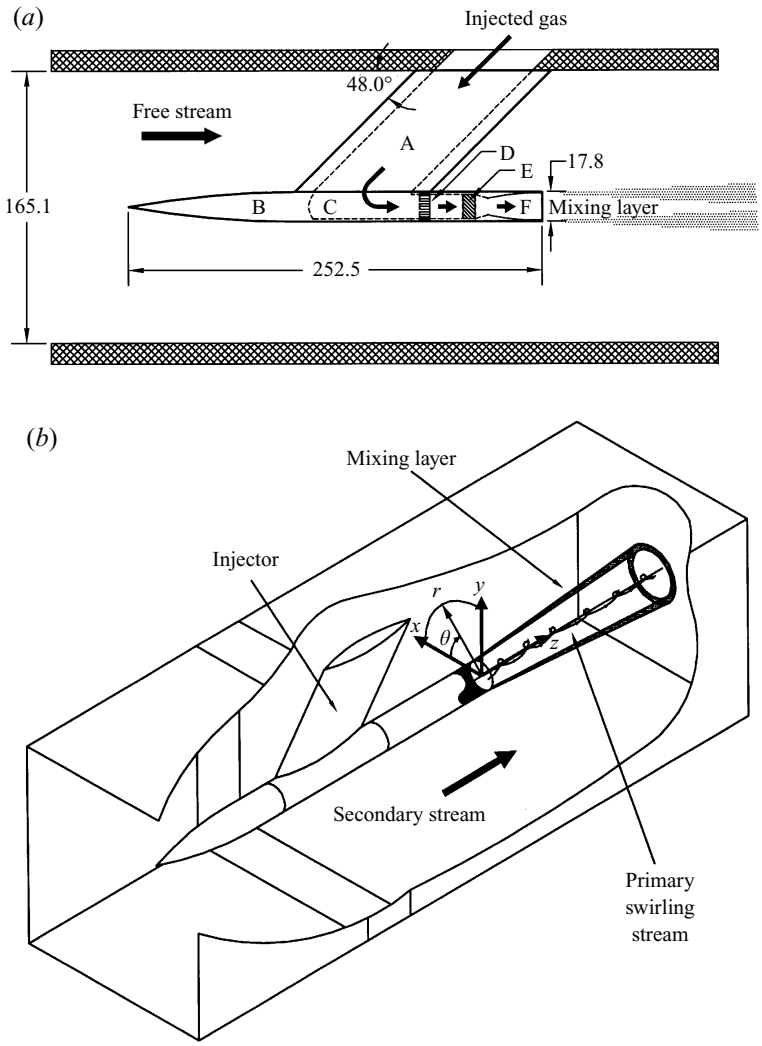

FIGURE 1. Schematics of the vortex injector (dimensions in mm). (*a*) The injector installed in the wind tunnel with the important components highlighted: A-strut, B-forebody, C-plenum, D-flow straightener, E-swirl vanes, F-nozzle. (*b*) The resulting flow field and associated coordinate system.

the wind tunnel in figure 1(*a*), consists of an ogive-cylinder forebody mounted on a hollow 8%-thick biconvex strut. The important components and dimensions of the injector are shown in the figure. High-pressure gas from the injection system flows through the hollow strut and into a plenum chamber. From there, it passes through a flow straightener, a set of swirl vanes, and finally through a converging–diverging (C-D) nozzle, which accelerates the gas to supersonic speed and forms the primary stream. Figure 1(*b*) shows a schematic of the resulting flow field and the Cartesian (x,y,z) and cylindrical (r,θ,z) coordinate systems used in this study.

An important consideration in mixing-layer development is the boundary layers that develop on the surfaces upstream of the mixing region. In the current study, the boundary layer on the internal nozzle walls was very thin due to the favourable pressure gradient therein. However, the boundary layer on the injector body, measured

from schlieren photographs, was shown to be approximately 3.5 mm thick for a secondary-stream Mach number (M_2) of 4.0. A simulation of a compressible boundary layer on a cylindrical body of the same length as the injector (25.3 cm) under the same free-stream conditions as those of the experiment was performed using the EDDY-BL code (Wilcox 1993). The results indicated a similar trailing-edge boundary layer thickness (3.28 mm) with a corresponding compressible displacement thickness (δ^*) and momentum thickness (θ) of 1.36 mm and 0.17 mm, respectively.

A critical aspect of the injector design was the interchangeable swirl vanes and C-D nozzles (Cattafesta 1992). The individual swirl vanes were stamped from brass sheets using a die fabricated by a numerically controlled milling machine. Each set of vanes was composed of 16 individual vanes affixed to a centrebody with epoxy. The four sets of vanes thus fabricated were designed to produce a tangential-velocity profile at the vane exit with $ru_\theta = K =$ constant (i.e. a free vortex), where r is the radius, and K is the circulation. The magnitude of the swirl for each set of vanes varied such that maximum flow angles of 15°, 30°, 45°, and 60° were obtained. The C-D nozzles were designed by an axisymmetric method-of-characteristics code for the ratio of specific heats $\gamma = 1.4$ and nominal Mach numbers of 2.5, 3.0, 3.5, and 4.0, and were fabricated using a computer-controlled lathe. In addition to their use with the vortex injector, the nozzles and vanes could be attached to the exit of the stilling chamber of the PSUFJF in order to create swirling free jets.

3. Instrumentation

The two facilities and the vortex injector described above were used to produce the several test cases that are presented in §4. In order to quantify both the mixing-layer growth rate and amount of swirl associated with each test case, several measurement techniques were employed. The mixing was quantified using a non-intrusive PLS technique, whereas the tangential-velocity profiles were measured using both LDV and intrusive probe surveys.

Two probes were necessary for the quantification of swirl strength. The first probe, a miniature fast-response conical five-hole probe, was used to measure Mach number, total pressure, and flow angularity. This probe was calibrated in air over the Mach number range of 1.5 to 4.0 and flow angles up to 25°. Since this calibration was only valid in air, this probe was used in air flows exclusively. Details of this probe's calibration and data-reduction technique are discussed in detail by Naughton, Cattafesta & Settles (1993*a*). The second probe, a miniature fast-response thermocouple, was used to measure the total-temperature distribution of the swirling flow fields. Knowledge of total temperature, which was expected to vary throughout the swirling jet and mixing layer (due to the difference in total temperature between the primary and secondary streams), was necessary for the calculation of velocity from the five-hole probe results. Since this probe actually measured a recovery temperature, the recovery factor was determined in air over the Mach number range 1.5 to 4.0. Further details of this probe are discussed by Naughton (1993).

These two probes were used to measure swirling air jets in the PSUSWT. Since the exact location of the jet axis was unknown, a square grid of points (typically 11×5) was taken that encompassed the core region. Using these data points, the jet axis (defined as the point in the swirling jet where both the radial and tangential velocities were zero) was located. Flow-field quantities along a radius from this location were then determined by interpolation. The estimates of uncertainty of these quantities

reflect the error due to this interpolation as well as those due to calibration and data-reduction errors.

In contrast to this method used for swirling air jets, the tangential-velocity profiles of the swirling helium and helium–nitrogen jets investigated in this study were determined using LDV in the PSUFJF facility. Special requirements for the LDV system were essential due to the large frequency bandwidth necessary to capture the Doppler signals associated with the large axial velocities of the helium jets. In addition, these signals tend to have low signal-to-noise ratios in supersonic flow. The best signal processor for resolving signals under such adverse conditions is believed to be the frequency-domain processor. The only such processor with sufficient bandwidth that was commercially available at the time of this study was the Doppler Signal Analyzer (DSA) manufactured by Aerometrics, Inc. A detailed description of this system and its operation is given by Cattafesta (1992).

LDV measurements of the tangential- and axial-velocity (u_θ and u_z) profiles at the nozzle exit were made using the fringes produced by the blue and green beams of an Argon-Ion laser. Light scattered by approximately 0.8 μm diameter silicon oil droplets was collected at a forward-scatter angle of 30° with respect to the optical axis. The velocity was sampled at several locations along a radius from the jet axis, although the radial extent was ultimately limited by oblique shocks emanating from the nozzle lip due to the overexpansion of the flow. In addition, measurements in the core of the swirling jet were not feasible because the seeding density there was too low to obtain a suitable sample size in the short run times available. Nonetheless, the location of the maximum tangential velocity in the swirling jet was determined for all the cases tested. The uncertainty estimates of these measurements include alignment error, finite-probe-volume effects, statistical error, and signal-processing resolution. Although velocity errors due to particle lag are normally cited as a source of error in such measurements, it has been shown to be negligible for the present case (Naughton, Cattafesta & Settles 1993*b*; Naughton 1993).

As opposed to the single-point measurements discussed above, the mixing-layer growth rate was determined using a planar technique. Probe measurements could have been used for this purpose, but the time required in a blow-down facility would have been too great for a detailed parametric investigation. Therefore, the PLS technique was chosen for its ability to survey the mixing layer non-intrusively in a short period of time while maintaining excellent spatial resolution. This technique has the added benefit of providing information about the turbulent structure in the mixing layer if a pulsed laser is used.

The use of planar light-scattering techniques for flow visualization is not recent. As early as 1961, McGregor visualized the flow over a delta wing using a sheet of light produced by a mercury lamp. However, beyond its use as a flow-visualization tool, this technique has also been used quantitatively to determine the concentration field. For example, Schneidermen & Sutton (1970) utilized a pulsed laser sheet to illuminate the smoke-seeded wake of a cone at Mach 2.5. From the recorded images, they then determined the mean values, r.m.s. fluctuations and turbulent spectra of the particle field. Another wake study (Bonnet & Chaput 1986) captured PLS photographs using a large-field camera. These photographs were subsequently digitized using a single photodiode mounted on a traversing mechanism. From these images they determined probability densities and evaluated the mixing. Recently, the availability of inexpensive image-processing equipment has made the detailed analysis of large ensembles of planar images feasible. Chao, Han & Jeng (1990) captured digitized images of a low-speed mixing layer, from which they calculated

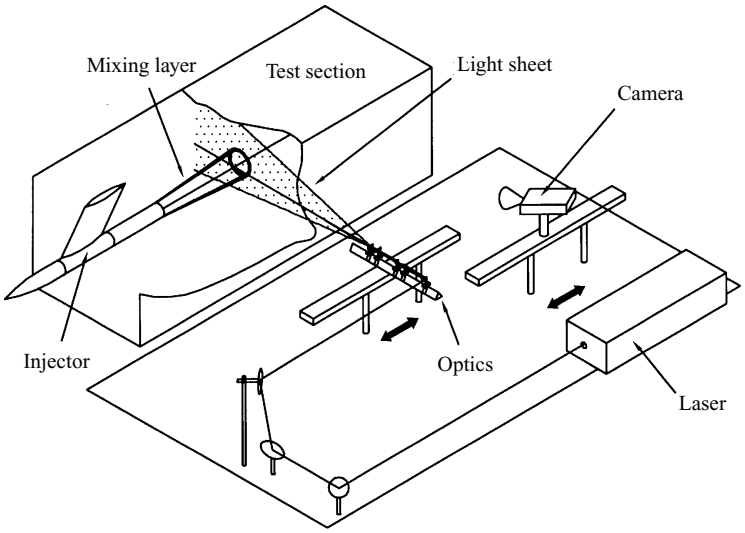

FIGURE 2. Planar laser scattering (PLS) implementation in the PSUSWT.

the concentration distribution and predicted the growth rate. In a study similar to the present investigation, Messersmith, Dutton & Krier (1991) used image processing to calculate the co-variance of the fluctuating intensity field in a compressible turbulent planar mixing layer. A comprehensive overview of planar image acquisition and analysis for turbulent flows is given by Prasad & Sreenivasan (1990).

The application of PLS to compressible turbulent mixing layers was previously investigated by Clemens & Mungal (1992). With this technique, they observed oblique structures in planar mixing layers at moderate convective Mach numbers that had previously gone undetected by path-integrating techniques such as shadowgraph and schlieren. Subsequently, Fourgette *et al.* (1991) and Naughton, Cattafesta & Settles (1989) applied this technique to axisymmetric compressible mixing layers resolving these flow fields with much greater detail than traditional point-wise measurements would have allowed.

The implementation of the PLS technique in the current study is shown in figure 2. The beam from a 10-W copper-vapour laser (10 kHz pulse rate, 1 mJ/pulse) was routed to an optical rail via mirrors. Mounted on the rail were two biconvex spherical lenses used to control the focus or minimum-sheet-thickness location, and two plano-convex cylindrical lenses used to control the divergence angle of the sheet. These optics produced either a horizontal (i.e. parallel to the x,z plane) or a vertical (i.e. perpendicular to the z-axis) light sheet that was less than 1 mm thick. The optical rail was attached to a stepper-motor-driven traversing mechanism allowing the light sheet to illuminate any location in the wind tunnel test section through transparent sidewalls. The camera used to image the light scattered from seed particles was located at a 45° angle to the wind tunnel axis and was mounted on a similar traversing mechanism. In the current test, the light sheet was located at the axial location of interest and approximately 100 images of a given axial location were recorded on Super-VHS videotape over the 3–5 s during which the vortex generator was operating.

For all cases tested here, the scattering particles were produced by the so-called 'passive-scalar' method (Clemens & Mungal 1992). Seeding of the secondary flow was

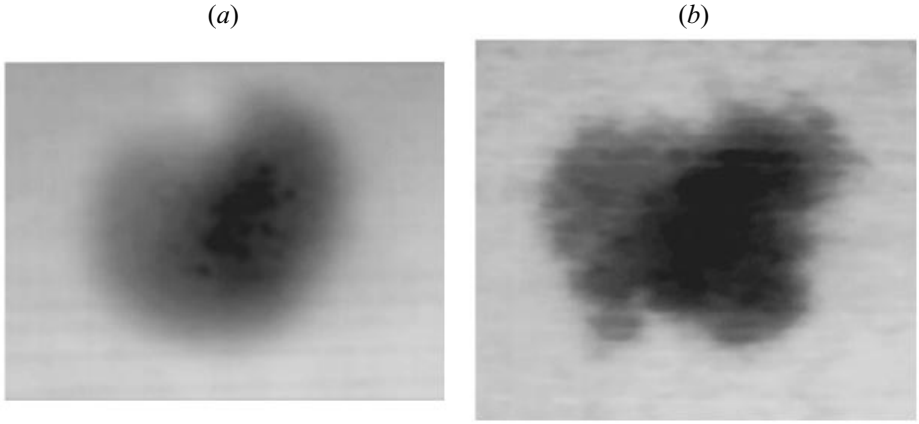

FIGURE 3. Planar (x-y) images of He–N_2/air swirling-jet flow field (case 4b) at $z/D_n = 9$. The result shown in (a) is a time-averaged image, whereas that in (b) is an instantaneous image.

accomplished by raising the moisture level of the supply reservoir somewhat above that used for normal tunnel operation. As this 'wet' air expanded through the wind tunnel nozzle, the static temperature dropped sufficiently to allow ice crystals to form, although no condensation shocks or flow distortion were observed. This ice-crystal formation process is complicated and is discussed in more detail by Wegener & Stein (1969). The seed particles thus formed have been measured to be 0.2 μm in diameter (Naughton *et al.* 1993*b*). Particles of this size have been shown to follow both the mean vortical flow (Maurice 1992; Naughton *et al.* 1993*b*; Naughton 1993) and the large-scale turbulent fluctuations (Naughton *et al.* 1993*b*; Samimy & Lele 1991).

Images capturing the effects of the mixing process were produced by ensuring that the injected primary stream was free of moisture. In this way, contrast was obtained between the seeded secondary stream, which scatters light and appears bright, and the dark unseeded primary stream. Time-averaged images, such as that shown in figure 3(a), were obtained by a conventional CCD camera that integrated scattered light from approximately 330 laser pulses over 1/30 s. In contrast, instantaneous images, such as that in figure 3(b), were produced by capturing scattered light due to a single 20 ns laser pulse with a gated image-intensified camera (Xybion Model ISG-250). The asymmetry evident in figure 3(a) was caused by vortices produced at the injector strut/forebody junction. Nevertheless, images such as these provided detailed information about the mixing layers of the cases studied here.

4. Test cases

The cases tested in the present study are summarized in table 1. The degree of compressibility and the amount of swirl for a given case are determined by the combination of nozzle, swirl vanes and injectant gas chosen. In this table, the compressibility is represented by $M_{c,1}$ calculated for the non-swirling jet, and the swirl is characterized by the vane angle and the estimated swirl number at the nozzle exit $\tilde{\tau}_n$ (details of the determination of $\tilde{\tau}_n$ are given in §5 and in Appendix A). Those cases using helium and helium–nitrogen (80%–20% mixture by volume) as injectant gases were selected to cover a broad range of these parameters. These cases cover moderate-to-high compressibility and weak-to-moderate swirl strengths. Because of the limited velocity data obtainable in the helium cases using LDV, additional cases

Case	M_1	M_2	Gas	Vane	$\tilde{\tau}_n$	$Re\,\mathrm{m}^{-1}$	ρ_2/ρ_1	$u_{2,z}/u_{1,z}$	$M_{c,1}$	Test
1*a*	3.0	4.0	He	0°	0.000	11.6×10^6	7.54	0.445	1.3	PLS, LDV
1*b*	3.0	4.0	He	30°	0.047					PLS, LDV
1*c*	3.0	4.0	He	45°	0.068					PLS, LDV
1*d*	3.0	4.0	He	60°	0.106					PLS, LDV
2*a*	3.7	4.0	He	0°	0.000	21.5×10^6	5.32	0.424	1.6	PLS
2*b*	3.7	4.0	He	45°	0.039					PLS
3*a*	4.5	4.0	He	0°	0.000	38.7×10^6	3.81	0.412	1.9	PLS
3*b*	4.5	4.0	He	45°	0.023					PLS
4*a*	2.8	4.0	He–N_2	0°	0.000	14.4×10^6	4.11	0.653	0.7	PLS, LDV
4*b*	2.8	4.0	He–N_2	0°	0.067					PLS, LDV
5*a*	2.6	2.5	Air	15°	0.017	60.7×10^6	0.957	0.983	≈ 0.0	PS
5*b*	2.6	2.5	Air	30°	0.042					PS
6*a*	3.1	3.0	Air	15°	0.009	56.7×10^6	0.958	0.989	≈ 0.0	PS
6*b*	3.1	3.0	Air	30°	0.023					PS
7*a*	3.6	3.5	Air	30°	0.014	63.3×10^6	0.961	0.992	≈ 0.0	PS
7*b*	3.6	3.5	Air	45°	0.020					PS
8*a*	4.0	4.0	Air	45°	0.014	68.8×10^6	0.963	0.994	≈ 0.0	PS
8*b*	4.0	4.0	Air	60°	0.021					PS

TABLE 1. Test matrix. PLS denotes planar laser scattering test in PSUSWT, LDV denotes laser Doppler velocimetry in PSUFJF, and PS denotes probe surveys in PSUSWT.

using air as the injectant were included in order to characterize the swirling flow produced by the vortex injector in more detail. Additional parameters calculated for the non-swirling cases using one-dimensional isentropic theory, including the density ratio, axial-velocity ratio, and Reynolds number, are also shown (these values are listed for the weaker of the two swirling jets in cases 5–8).

For all cases run in the wind tunnel (those indicated by a PLS or PS in table 1), the injector total pressure was adjusted such that the static pressure at the injector nozzle exit was approximately the same as that of the secondary flow (i.e. fully expanded nozzle exit conditions). In the cases with swirl, this was accomplished by matching the pressure at the edge of the primary flow with that of the secondary flow, since the static pressure varies with radius in the swirling primary flow. For these cases, the pressure was set at the value used for the non-swirling jet (determined from the isentropic relations) and then slightly varied to minimize the shock strength emanating from the nozzle lip. In contrast, the cases that were run in the free-jet facility (denoted by LDV in table 1) had their stagnation pressure set at a level such that a normal shock appeared just outside the nozzle exit, but at a location downstream of the LDV probe volume. This over-expanded condition was chosen in order to conserve helium and extend run times.

For all the cases where mixing-layer growth rates were determined (cases indicated by PLS in table 1), it is important to consider the state of the mixing layer at the measurement points. Several different criteria have been suggested as means of determining if the mixing layer has achieved a fully developed state. This state is

attained at the location (z/D_n) where the mean velocity and the turbulent quantities (e.g. Reynolds stress) become self-similar. In practice growth rates are often determined from points measured in the region where only the mean velocity profile is self-similar. Bradshaw (1966) experimentally determined that the mixing layer originating from an axisymmetric jet with a laminar incoming boundary layer required a distance corresponding to $Re_l = \rho_1 u_1 l/\mu_1 = 7 \times 10^5$ for self-similarity. For mixing layers originating from turbulent boundary layers, Bradshaw (1966) suggested that distances up to $l = 1000\theta$ might be necessary for self-similarity. For compressible turbulent planar mixing layers, Goebel & Dutton (1991) found that experimental data indicated that the criterion for self-similarity was given by a Reynolds number based on the mixing layer thickness $Re_\delta = \bar{\rho}(u_1 - u_2)\delta/\bar{\mu}$, where $\bar{\rho}$ is the average density, $\bar{\mu}$ is the average viscosity of the two streams, and δ is the mixing-layer thickness (Goebel & Dutton 1991 used the 80%-velocity thickness for δ, but since we are only estimating Re_δ any thickness of the same order should be appropriate). They derived the value of Re_δ for the two-component mixing layer using the Re_l criterion from Bradshaw's axisymmetric jet analysis and found that a value of 1×10^5 was required for self-similarity. These criteria are conservative for mixing layers with high shear, such as those in the current study, which erase the initial momentum deficit extremely rapidly (Goebel & Dutton 1991).

The growth rates of the mixing layers in the current study were determined from points ($z/D_n > 3.0$) that met the Re_l and Re_δ criteria (where Re_l is now defined as $Re_l = \bar{\rho}(u_1 - u_2)l/\bar{\mu}$ for this co-flowing case). However, they do not meet the momentum thickness requirement until farther downstream. However, the momentum thickness criterion was postulated as the distance that might be required for self-similarity in full-scale situations such as in base flows or flows issuing from long jet pipes. Such flows have boundary-layer effects which are equivalent to (and can be greater than) the dimension of the jet itself, and thus this criterion seems too restrictive for this case. Therefore, we believe that it is safe to presume that the mixing layers of the current study were sufficiently developed at the measurement locations used.

5. Swirling-jet flow-field results

As previously discussed, probe surveys of the swirling air jets were made in order to characterize the swirling flows produced by the vortex injector. The mixing layers of these air flows were dominated by the injector boundary layer (due to the small velocity gradient across the mixing layer), and thus, in this respect, were not of interest. Figure 4(*a*) shows a typical radial distribution of u_x and u_y derived from the surveys from case 6*b*, while figure 4(*b*) shows the axial velocity u_z for the same case. For an axisymmetric flow, u_x is analogous to the radial velocity, and the tangential velocity corresponds to $|u_y|$. These surveys reveal that this swirling jet has a maximum tangential velocity ($\approx$100 m s^{-1}) that is significant fraction of the axial velocity ($\approx$625 m s^{-1}), and a slightly negative radial velocity near the core. The total temperature also exhibited a radial variation in the core region, a common characteristic of compressible vortices. This is the so-called 'energy separation' or Ranque–Hilsch effect (Hilsch 1947; Hartnett & Eckert 1957).

The data from cases 5–8 all exhibited features similar to those in figure 4. A discussion of the structural details of these swirling jets is beyond the scope of the present paper, but they are discussed by Cattafesta (1992) and are the subject of a

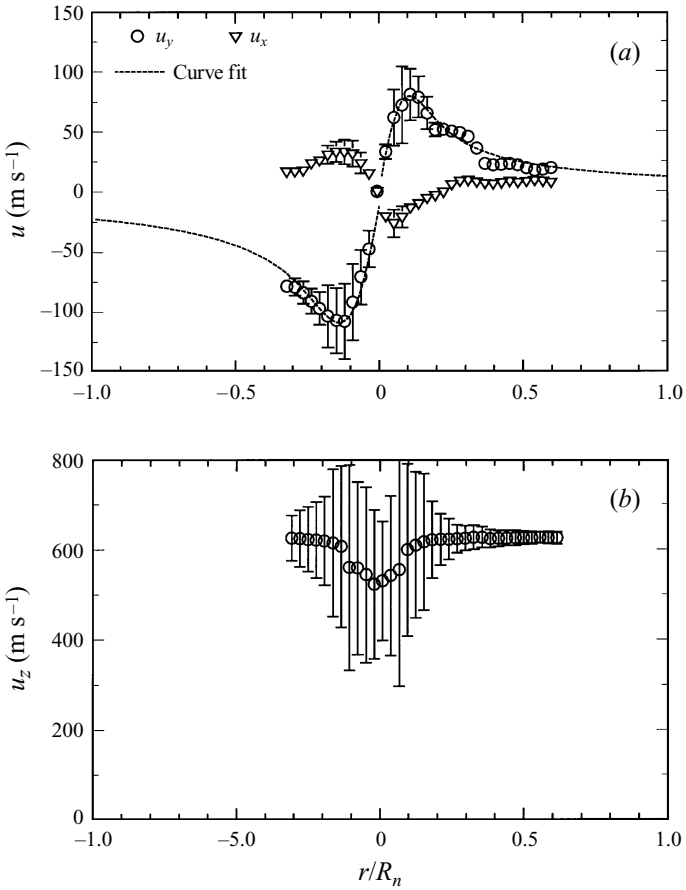

FIGURE 4. Velocities as a function of non-dimensional radial position for a typical swirling jet (case 6*b*): (*a*) u_x and u_y, and (*b*) u_z.

future publication. Nonetheless, a summary of those features relevant to the current study, in particular the quantification of swirl strength, is presented below.

The line in figure 4(*a*) is a least-squares fit to the u_θ-data points using an equation of the form

$$u_\theta = (k_t/r)\left(1 - \exp\left\{-r^2/r_t^2\right\}\right), \tag{5.1}$$

where k_t and r_t are a characteristic vortex strength and length scale, respectively, which are parameters determined by the fit. The data and this curve fit suggest a multi-layered structure, which is known to be a characteristic of compressible vortices (Délery *et al.* 1984; Metwally, Settles & Horstman 1989; Mandella & Bershader 1987; Cattafesta 1992). The inner-core region exhibits solid-body rotation with a tangential velocity $u_\theta \propto r$, the outer portion behaves like a 'free' vortex with $u_\theta \propto r^{-1}$, and the region in between functions as an 'overlap' region.

To investigate this further, the circulation ($k = ru_\theta$) non-dimensionalized by the vortex strength parameter k_t was plotted against (r/r_t) for all the present swirling air jet cases. As shown in figure 5, the data of the present study collapse toward a single curve (not shown) when plotted in this manner. The form of this line is given by

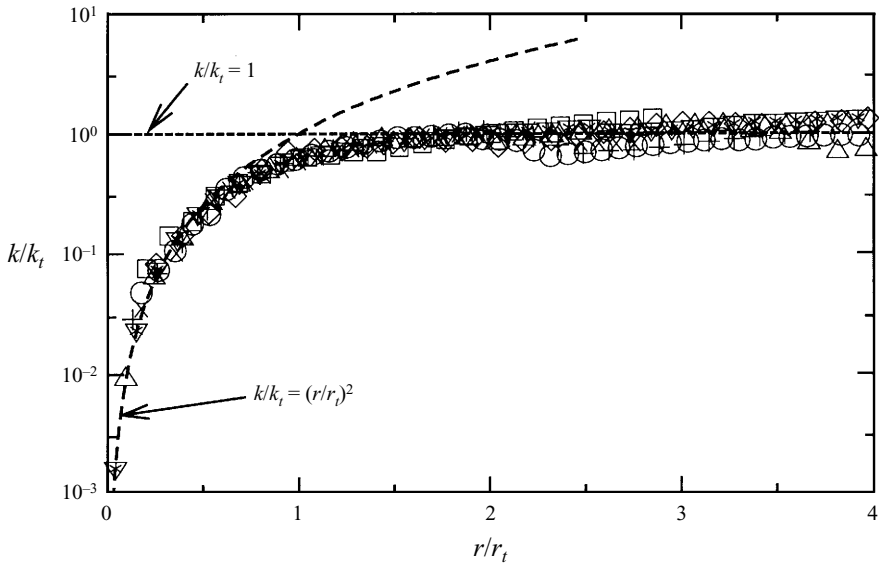

FIGURE 5. Non-dimensional circulation profiles for the swirling air jet cases: ◯, case 5*a*; ▽, case 5*b*; □, case 6*a*; △, case 6*b*; ◇, case 7*a*; *, case 7*b*; +, case 8*a*; ×, case 8*b*. The long-dashed line is the inner-region solution while the short-dashed line is the outer-region solution.

rearranging (5.1):

$$k/k_t = \left(1 - \exp\left\{-r^2/r_t^2\right\}\right). \tag{5.2}$$

The curve $k/k_t = (r/r_t)^2$ (long-dashed line) is the solution of (5.2) for small r and represents solid-body rotation, whereas the curve $k/k_t = 1$ (short-dashed line) is the form of (5.2) for large r and represents a free vortex (circulation constant). It is clear from this figure that the current swirling air jets have the characteristic three-layer structure common to turbulent vortices.

In addition to this evidence, LDV measurements (Cattafesta 1992) of swirling jets similar to those in cases 5–8 indicated that high levels of turbulence were present in the core, a characteristic also common to incompressible swirling flows generated by various means (Délery *et al.* 1984; Bandyopadhyay, Stead & Ash 1991). The core turbulence quantities measured by Cattafesta (1992) are very similar to those observed in the wake of an axisymmetric body (Chevray 1968) with the exception of the persistence of significant turbulence levels at larger distances from the axis. This suggests that the observed core turbulence is generated by the swirl vanes' centrebody, whereas the turbulence outside the core is due to other sources such as the wakes from the vanes themselves. This does not preclude the possibility that some of the turbulence observed in these swirling jets is due to the mean strain caused by the tangential-velocity profile. Regardless of the source of the turbulence, we believe that the swirling jets investigated in the current study have turbulence distributions similar to those of other such swirling flows.

Owing to cost limitations, measurements of all the helium swirling jets were not possible. However, the swirling air jet results led us to believe that the limited LDV data obtained for cases 1 and 4 could be used to estimate the swirl in those cases where it was not measured. The means by which an estimated swirl number at the nozzle exit $\tilde{\tau}_n$ is calculated from the available measurements is described in detail in Appendix A.

Case	M_1	M_2	Gas	Vane	$\tilde{\tau}_n$	ρ_2/ρ_1	$u_{2,z}/u_{1,z}$	M_c	δ'_c	$\delta'_{c,i}$
1*a*	3.0	4.0	He	0°	0.000	7.54	0.445	1.3	0.0065	0.0320
1*b*	3.0	4.0	He	30°	0.047				0.0088	
1*c*	3.0	4.0	He	45°	0.068				0.0091	
1*d*	3.0	4.0	He	60°	0.106				0.0108	
2*a*	3.7	4.0	He	0°	0.000	5.32	0.424	1.6	0.0063	0.0329
2*b*	3.7	4.0	He	45°	0.039				0.0094	
3*a*	4.5	4.0	He	0°	0.000	3.81	0.412	1.9	0.0080	0.0331
3*b*	4.5	4.0	He	45°	0.023				0.0087	
4*a*	2.8	4.0	He–N_2	0°	0.000	4.11	0.653	0.7	0.0062	0.0159
4*b*	2.8	4.0	He–N_2	45°	0.067				0.0091	

TABLE 2. Summary of swirl numbers and mixing-layer growth rates

In short, the swirl number τ used to characterize the strength of the swirling jets in this study is given by

$$\tau = \frac{H_z}{F_z R} = \left[2\pi \int_0^R \rho u_\theta u_z r^2 \mathrm{d}r\right]\left[2\pi R \int_0^R \rho u_z{}^2 r \mathrm{d}r\right]^{-1}, \tag{5.3}$$

where H_z is the axial component of angular momentum flux, F_z is the axial component of linear momentum flux, R is the radius over which the integration is performed, and ρ is the density. To evaluate this integral at any location, the variables on the right-hand side of the equation must be known as a function of r. This integral was first evaluated at the nozzle exit for those cases where data were available. This information was then used to generalize the swirl produced by a given set of vanes. Having characterized each set of vanes, the swirl number at the nozzle exit was estimated with a typical accuracy of $\pm$ 15% (see Appendix A for details). This estimated swirl number ($\tilde{\tau}_n$) for cases 1–4 is given in table 2.

Although the swirl number τ characterizes the swirling jets in the present study, it is an integral quantity. It has been shown that, in incompressible swirling flows, swirling jets with the same value of τ given by (5.3) but with very different tangential-velocity profiles evolve differently in the near field ($z/D_n < 5$) (Farokhi, Taghavi & Rice 1989). In certain applications, other swirl parameters based on local quantities may be more appropriate to quantify swirl. For instance, Lessen, Singh & Paillet (1974) found that the inviscid stability of a swirling wake depends on the ratio of the maximum tangential velocity to the maximum axial velocity deficit. As will be discussed in §9, the mixing-layer growth rate of swirling jets appears to be controlled by, among other parameters, the ratio of the tangential velocity at the jet boundary to the axial velocity there. Thus, a full characterization of a swirling flow requires a detailed knowledge of both the axial- and tangential-velocity profiles. For previously stated reasons, obtaining such data for the present helium and helium–nitrogen cases was not possible. Nonetheless, the swirl number τ provides at least a first-order estimate of the strength of the swirling jets in this study. Furthermore, since all the swirling cases in this study are expected to have a tangential-velocity profile given by (5.1), other swirl number definitions, both local and integral, should scale similarly to τ.

6. Mixing-layer growth-rate analysis and results

The raw PLS images captured by the methods described in §3 were analysed to extract quantitative data. Specifically, the images were used to determine mixing-layer growth rates. In addition, the instantaneous images were also examined for any turbulence information that they might contain. Prior to these analyses, all images (time-averaged and instantaneous) were spatially transformed to correct for the viewing angle of the camera and were spatially filtered to eliminate high-frequency noise.

In order to determine the mixing-layer growth rates of the test cases listed in table 1, the mixing-layer concentration thickness δ_c was determined at several axial locations. The definition of δ_c and its determination are discussed in Appendix B. Figure 6 shows the δ_c-values determined at several streamwise locations for cases 1*a*–1*d*. The error bars of the δ_c-values shown include contributions from light-sheet intensity variations, electronic imaging noise, and data-reduction error. The slopes of the least-square-fit lines connecting the individual δ_c points are the mixing-layer growth rates. The growth rates δ_c' thus determined are summarized in table 2 for the cases of this study.

It is evident in figure 6 that the data points at z/D_n=9 are all low, although the predicted thickness (shown by the lines) passes well within the uncertainty of the points. Similar results are observed for the other cases as well. Two possible causes of these low values are suggested. The first is that tunnel sidewall reflection of laser light affects the images at this location. This would cause a change in the mixing-layer thickness values calculated from these images. However, it is more likely that a weak wave passes through the mixing layer somewhere in this vicinity. Although the shock waves from the injector nose would pass through the jet axis only downstream of z/D_n=12 (i.e. downstream of the location where experimental images were obtained), a weak wave from the strut/ceiling interface is observed crossing the jet axis at $z/D_n \approx 10$. Whatever the cause, the effect is small, and the jet appears to recover its normal growth by z/D_n=12.

An interesting feature of figure 6 is that the mixing-layer thickness does not extrapolate to zero at the nozzle exit. Since there was a boundary layer on the injector body of approximately 3.5 mm, this virtual-origin effect is expected. This boundary layer will create a seeding-density distribution at the nozzle exit. However, as discussed in §4, the mixing-layer growth rate should be unaffected by these incoming conditions at the first measurement location $z/D_n = 3$.

As an accuracy check of the method used herein to determine growth rates, the data for the present non-swirling cases were compared with those obtained by other researchers. For this comparison, the non-swirling mixing-layer growth rates were non-dimensionalized by their incompressible growth rate value δ_i'. The form of δ_i' is given by Papamoschou & Roshko (1988) as

$$\delta_i' = K(1-R)(1+S^{1/2})/(1+RS^{1/2}), \tag{6.1}$$

where K is a constant that depends on the method used to determine the mixing-layer thickness. In order to determine the value of K for the concentration thickness used in this study, a hyperbolic-tangent concentration profile was assumed, from which $K = 0.035$ was determined. This constant was evaluated in a similar way to that which Papamoschou & Roshko (1988) used to determine the value of K for growth rates based on Pitot thickness. The incompressible concentration mixing-layer growth rate $\delta_{c,i}'$ calculated for the same values of R and S as those in the present study are

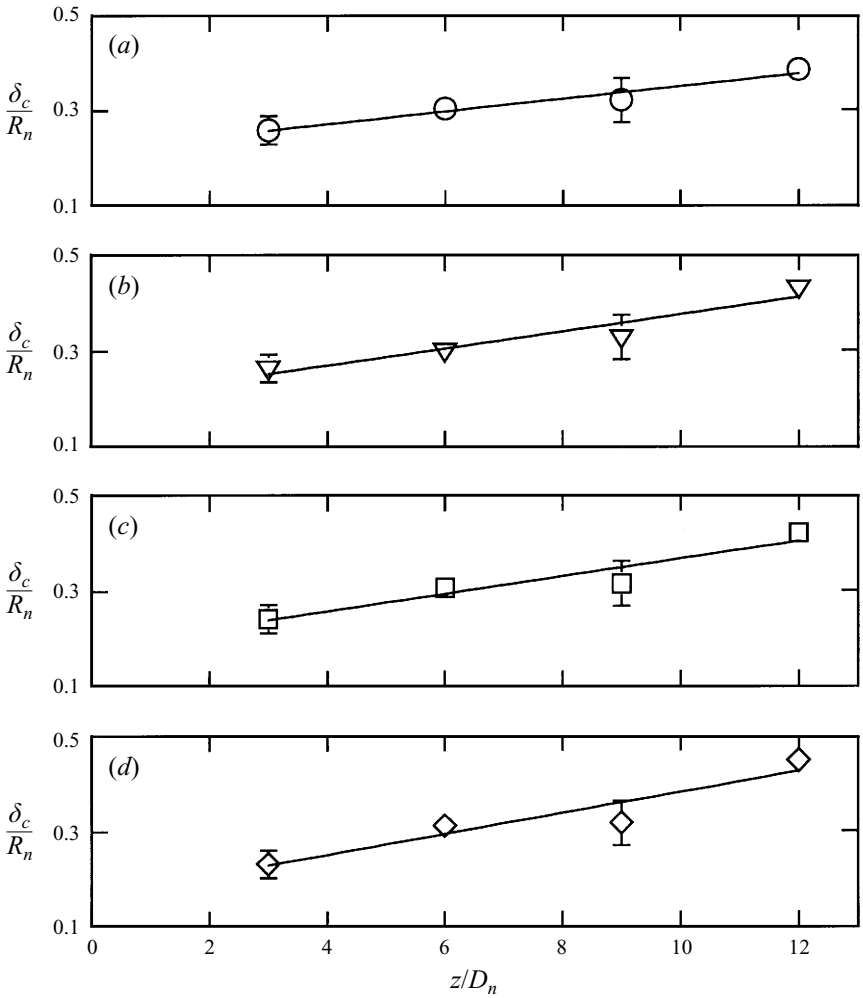

FIGURE 6. Mixing-layer thicknesses at several axial locations for a helium/air case with various degrees of swirl: (*a*) case 1*a* (no swirl); (*b*) case 1*b*; (*c*) case 1*c*; and (*d*) case 1*d* (highest swirl).

also listed in table 2. Figure 7 shows the non-dimensionalized mixing-layer growth rates $\delta_c'/\delta_{c,i}'$ for the non-swirling cases of the current study plotted with δ'/δ_i'-values determined from other studies. Note that the non-dimensionalization takes into account the technique used to determine the mixing-layer growth rate, and thus the scatter is due to experimental uncertainties and not the various techniques used. Nonetheless, the non-swirling data of the current study fall within this scatter, and thus it may be concluded that the present method for estimating growth rates is valid.

However, is it possible that growth rates are incorrectly estimated when mean imaging data are used to determine turbulent mixing? To answer this question, a series of instantaneous images taken under the same conditions and at the same axial location was analysed using the growth-rate determination method presented in Appendix B. After determining the δ-value for each of these instantaneous images, an average δ was calculated. This average mixing-layer thickness was found to be essentially identical to that determined from a single time-averaged image of the same location under the same conditions. This is an important result in that, for the

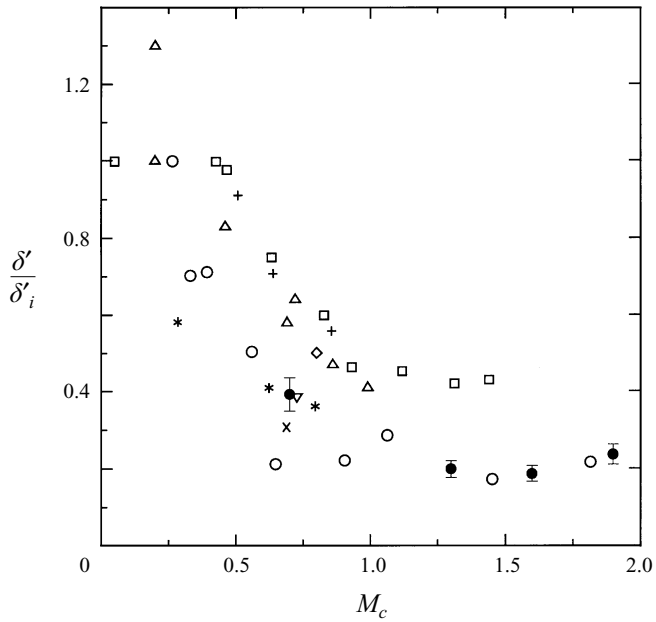

FIGURE 7. Non-swirling jet non-dimensional mixing-layer growth-rate data plotted versus convective Mach number. The data in the figure include results from the following planar mixing layer studies: ○, Pitot thickness, Papamoschou & Roshko (1988); ∗, visual thickness, Clemens & Mungal (1992); □, vorticity thickness, Bogdanoff compilation (1983); △, velocity thickness, Goebel & Dutton (1991); ◇, vorticity thickness, Gruber *et al.* (1992); and +, vorticity thickness, Elliot & Samimy (1990). In addition, the following data from axisymmetric studies are also shown: •, concentration thickness, the present study; ▽, Pitot thickness, Fourgette *et al.* (1992); and ×, visual thickness, Fourgette *et al.* (1992).

present cases, it demonstrates that the mean images do not overestimate mixing due to a flapping motion of the boundary that could occur between the two essentially unmixed streams.

Turning to the mixing-layer growth-rate results of the swirling cases, it is found that these flows mix at a higher rate than their non-swirling counterparts. Figure 8 shows a swirl-induced mixing enhancement parameter, the ratio of the mixing-layer growth rate for a swirling jet $\delta'_{c,s}$ to that of the corresponding non-swirling case $\delta'_{c,j}$, plotted versus the estimated swirl number at the nozzle exit $\tilde{\tau}_n$. The vertical error bars shown in the figure are estimated using the estimated uncertainties of the δ_c-values (Bowker & Liebermann 1972, p. 336). Although the uncertainty is large, the degree of mixing enhancement clearly increases with the magnitude of swirl. Moreover, for the cases shown, compressibility does not appear to affect the enhancement significantly, although this aspect will be discussed further in §9. An alternative interpretation of these results is that the mixing layer of a swirling jet has a growth rate equivalent to that of a non-swirling jet (with equivalent values of R and S) at a lower level of compressibility.

7. Turbulent structure analysis and results

The growth-rate analysis described in the previous section was chiefly applied to the time-averaged images in order to evaluate the effect of swirl on mixing. However, the discovery of swirl-enhanced mixing-layer growth prompted us to examine instan-

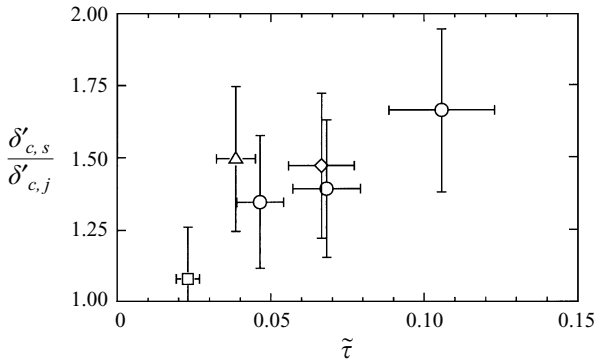

FIGURE 8. Mixing-layer growth-rate enhancement data of the present study plotted versus swirl number: ○, case 1, $M_{c,1}$=1.3; △, case 2, $M_{c,1}$=1.6; □, case 3, $M_{c,1}$=1.9; and ◇, case 4, $M_{c,1}$=0.7.

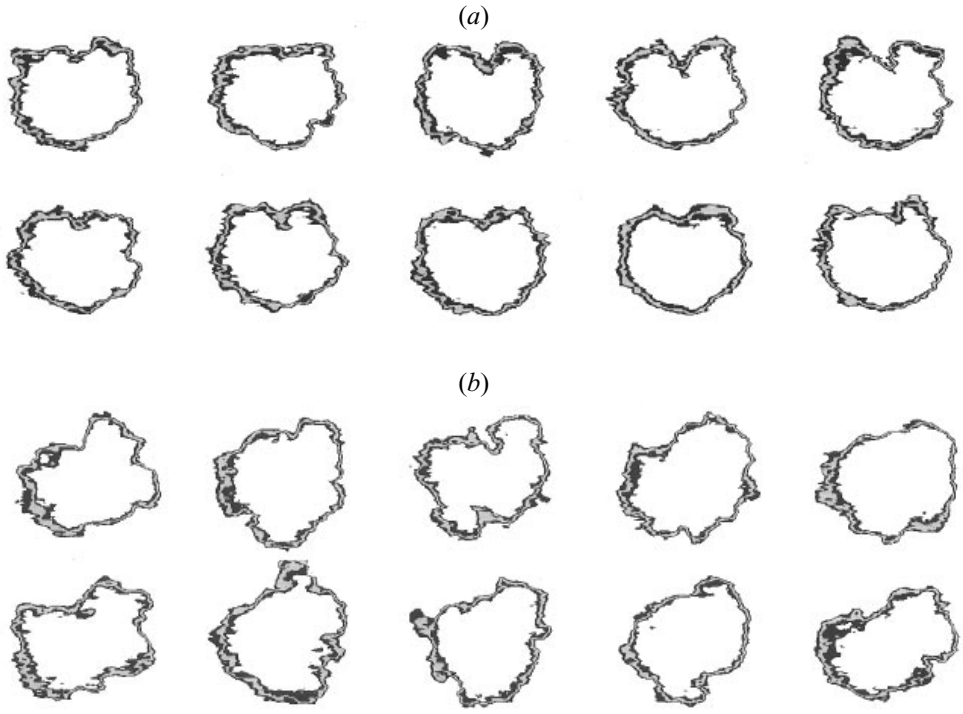

FIGURE 9. Enhanced instantaneous images of the He–N_2/air case at $z/D_n = 12$: (*a*) non-swirling jet, case 4*a*, and (*b*) swirling jet, case 4*b*.

taneous PLS images for clues to its cause. Visual inspection of the raw instantaneous image data revealed observable differences between the mixing layers of the swirling and non-swirling jets. Several randomly chosen instantaneous images in which the mixing layer has been enhanced are shown in figures 9(*a*) and 9(*b*) for cases 1*a* and *d*, respectively, at $z/D_n = 12.0$. These images suggest that structures in the mixing layer of the swirling jet are more widely varied in shape and extend further from

the axis than those of their non-swirling counterparts. The enhancement technique used with these images was tailored to highlight the mixing layer, and thus the results should be viewed as providing only qualitative information about the structure therein. Nonetheless, they sufficiently demonstrate that large-scale structures, akin to those that are responsible for the engulfment process in incompressible mixing layers, occur in the swirling jet but are noticeably absent in images shown of the non-swirling jet.

To quantify these observed differences, two techniques were used involving a series of instantaneous images such as these. The first technique determined the intermittency of the intensity at a given point, while the second technique evaluated the r.m.s.-intensity fluctuation levels. In the present context, the intermittency ι is defined as the fraction of time during which a given spatial location lies in the 'mixed' fluid region,

$$\iota = \mathrm{P}(I_l^* < I^*(r,\theta,z) < I_h^*), \tag{7.1}$$

where I^* is a normalized intensity (see Appendix B for its definition), P is the probability of the expression in parentheses, and I_l^* and I_h^* are normalized-intensity values representing the boundary of the mixing layer. The process used to determine ι in the current study is discussed in Appendix B. Figure 10(*a*) shows the radial distribution of the intermittency for case 4*a*. Note that the intermittency is zero outside the mixing layer and peaks at a value of unity inside the mixing layer. To characterize the extent of the mixing layer, the non-dimensional full-width half-maximum value ($\Delta r_{\mathrm{FWHM}}/R_n$) is determined. The uncertainty of the intermittency is dominated by the statistical error of calculating a percentage from a finite sample (Bowker & Liebermann 1972, p. 466).

A typical radial distribution of the normalized-r.m.s. (σ_I^*) intensity that was derived from the series of instantaneous images that produced figure 10(*a*) is shown in figure 10(*b*). The quantity σ_I^* described in Appendix B, is the r.m.s.-fluctuating intensity normalized by the mean intensity of the unmixed secondary flow. The error bars represent statistical uncertainties. Note that the normalized-r.m.s. intensity σ_I^* peaks in the central portion of the mixing layer and falls off to finite values in the primary and secondary streams. The higher value of σ_I^* in the secondary stream does not necessarily imply that there are greater turbulence levels there, but rather reflects the higher photon-shot noise in the seeded stream compared to the unseeded stream. Although the noise level is high in these results, the peak values of σ_I^* are clearly above the noise, and thus such results are useful for comparisons of the swirling and non-swirling cases.

Applying these techniques to the cases of this study reveals several differences between the swirling and non-swirling cases. As an example, the raw r.m.s. intensities (σ_I) of two He–N_2/air cases are shown in figure 11. The grey-levels shown in these images are proportional to the σ_I-values calculated from a series of raw images, the darker shades indicating those regions with the largest fluctuations. Although the r.m.s.-intensity values represented here have not been corrected for illumination variation, it is still evident that there is a significant difference in the turbulence levels between the swirling (*e–h*) and non-swirling (*a–d*) cases for $z/D_n > 6$. To investigate this more closely, individual radial cuts through the bottom of the shear layer ($\theta = -90^\circ$) are considered next.

Figures 12(*a*) and 12(*b*) present the normalized-r.m.s.-intensity fluctuations (σ_I^*) for the He–N_2/air non-swirling and swirling cases, respectively. These results indicate that the fluctuations are small for both the swirling and non-swirling cases at $z/D_n = 3$

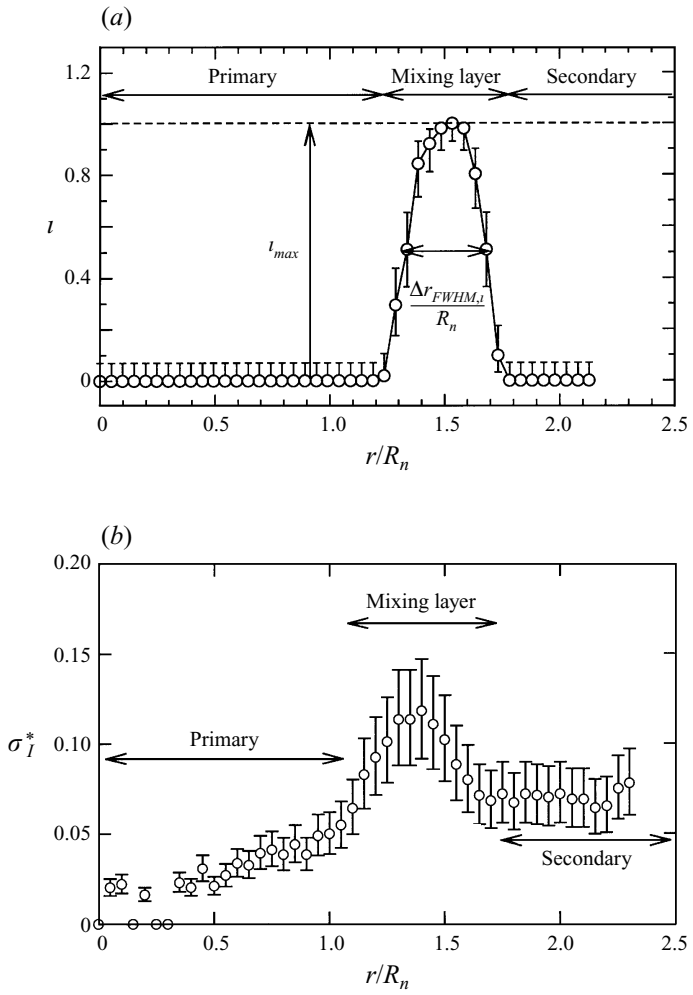

FIGURE 10. Turbulence quantities along a radius at $\theta = 0°$ derived from an ensemble of 50 instantaneous images of the non-swirling He–N_2/air case (case 4*a*) at $z/D_n = 9$: (*a*) intermittency; and (*b*) normalized-fluctuating intensity.

and 6, and that there is little difference between them. However, at axial locations further downstream, the mixing layer becomes distinguishable as a region of higher σ_I^*-values near the peak in the σ_I^*-distribution. From the figure, it is clear that both the magnitude and radial extent of this region are greater for the swirling case.

The results of the intermittency analysis of case 4, shown in figures 12(*c*) and 12(*d*), concur with these findings. The figures reveal that, for $z/D_n < 6$, the intermittent region is indistinguishable for the two cases. However, at axial locations further downstream, the intermittent region of the swirling jet grows wider, and, at $z/D_n = 12$, the peak drops below unity. Recalling the definition of intermittency given by (7.1), this latter result indicates that the engulfment processes in the mixing layer are carrying unmixed fluid at least as far as the central portion of the mixing layer. In contrast, the intermittency profile of the non-swirling case changes little over the entire axial region shown. These quantitative results indicate that the apparent differences in turbulent structure observed in the raw instantaneous images of the swirling jet

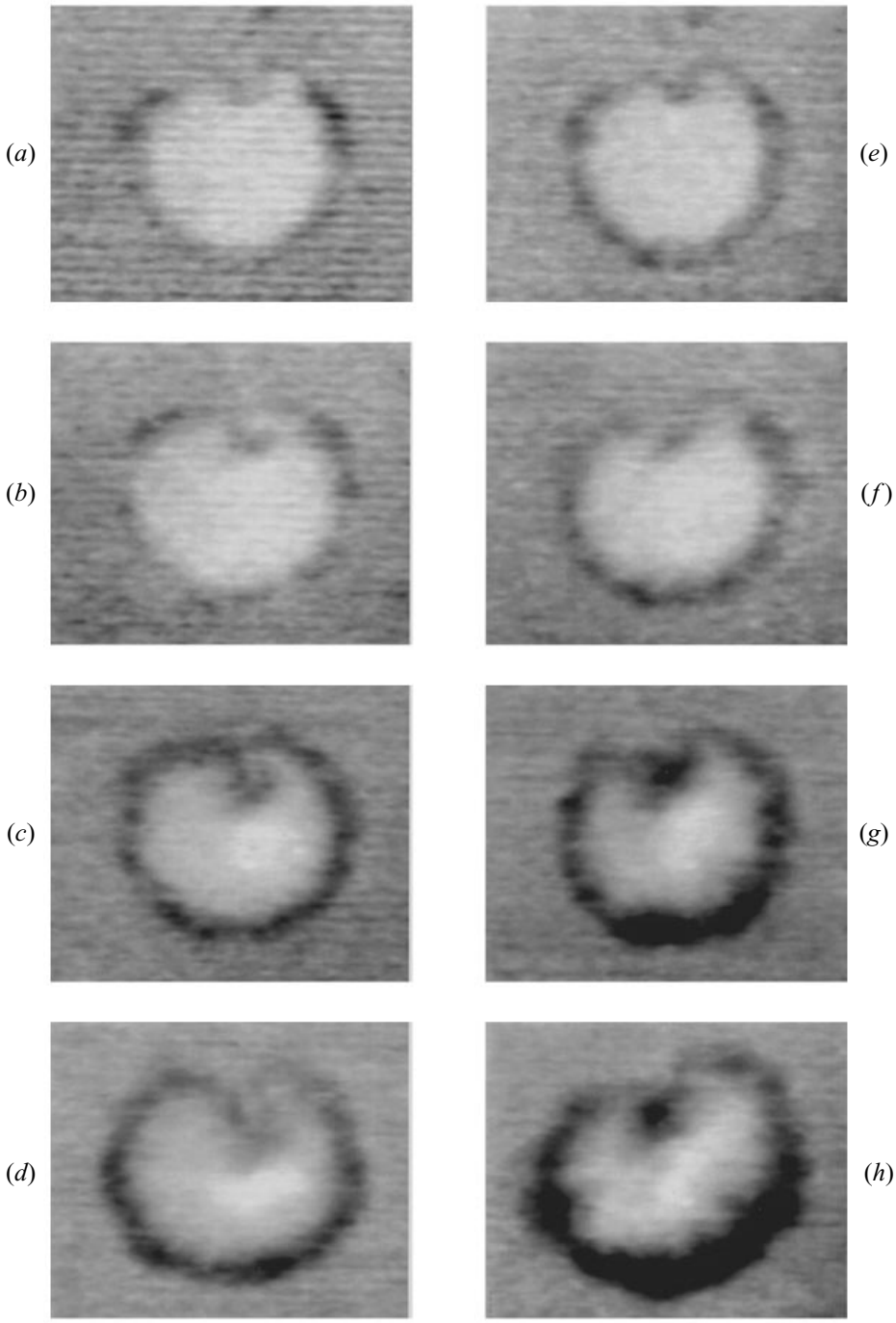

FIGURE 11. Images of uncorrected r.m.s. intensity fluctuations in the (x,y)-plane for the He–N_2/air case: (*a–d*) case 4*a*, non-swirling case, at $z/D_n = 3.0$, 6.0, 9.0 and 12.0, respectively (top to bottom); and (*e–h*) case 4*b*, swirling case, at $z/D_n = 3.0$, 6.0, 9.0 and 12.0. The regions of higher fluctuations are indicated by the darker shades.

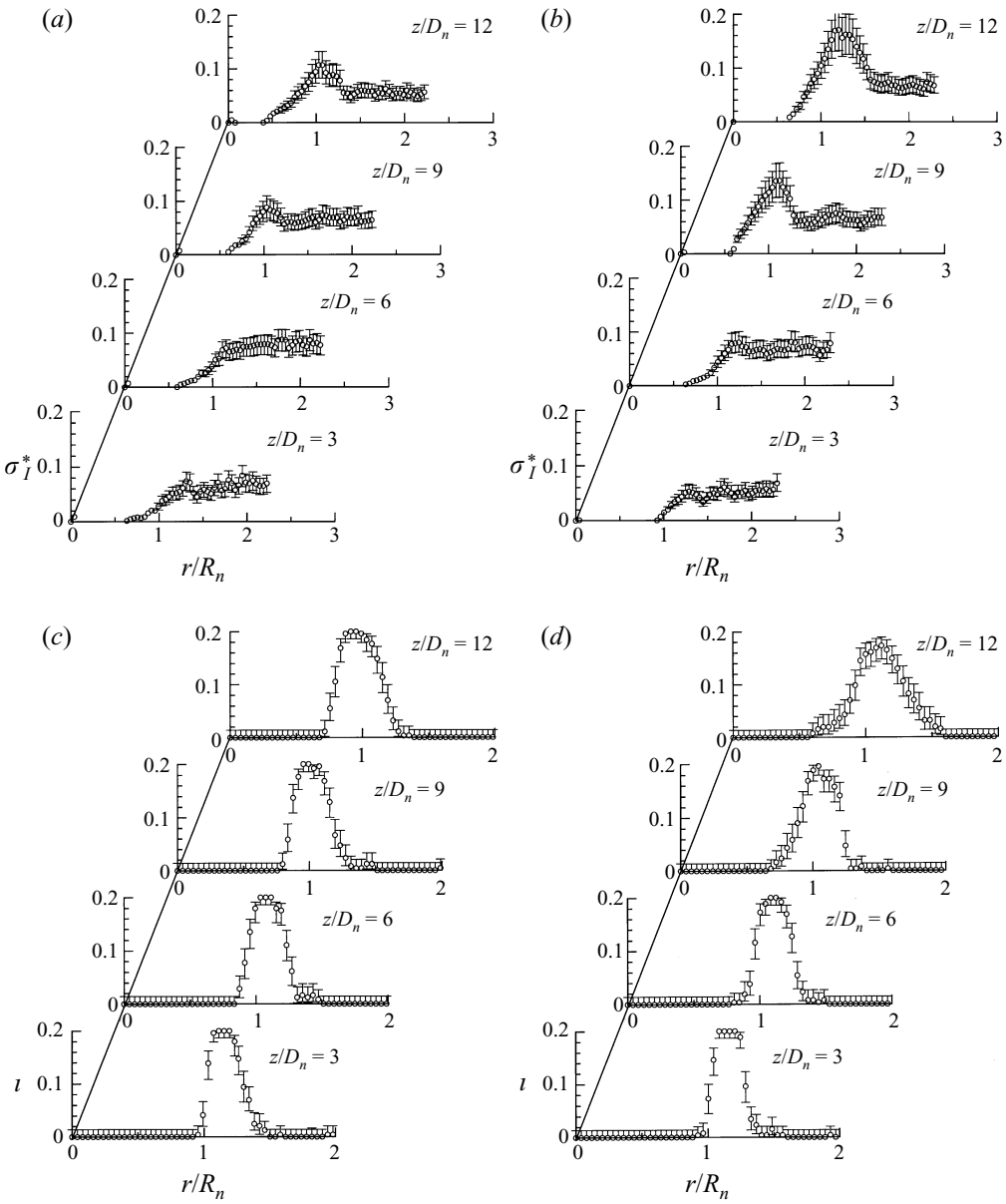

FIGURE 12. Radial distribution of turbulence quantities at $\theta = -90°$ for the He–N_2/air case at several axial locations: normalized-rms intensity fluctuations for (*a*) non-swirling jet, case 4*a* and (*b*) swirling jet, case 4*b*; and intermittency of (*c*) non-swirling jet, case 4*a* and (*d*) swirling jet, case 4*b*.

are caused by turbulent fluctuations of greater magnitude and extent than those of its non-swirling counterpart. Since the cases with greater fluctuations correspond to those with higher growth rates, it appears reasonable to assume that the addition of swirl produces higher turbulence levels, thus resulting in the increased entrainment and the higher mixing-layer growth rates previously observed.

To further examine the link between the turbulence and the increased growth rates observed, the full-width half-maximum values determined from the intermittency

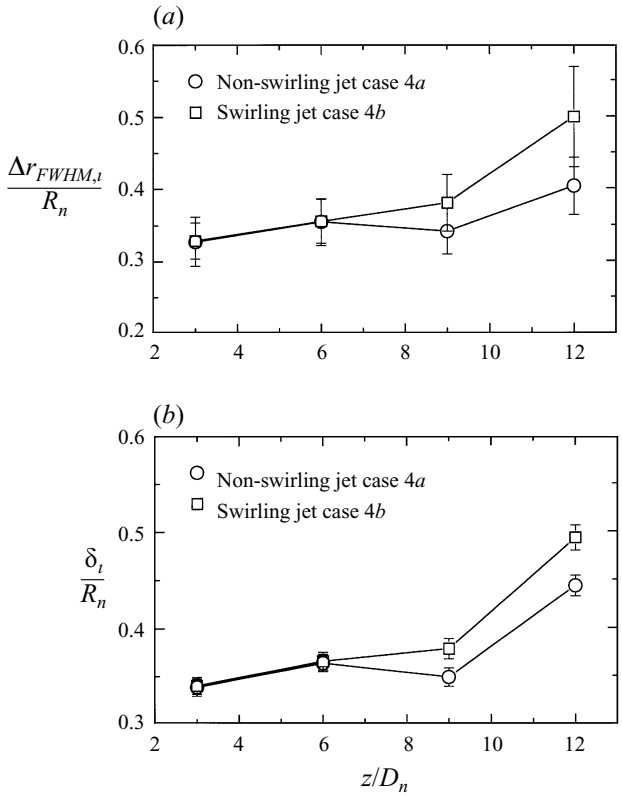

FIGURE 13. Characteristic length scales calculated from the intermittency distributions for the He–N_2/air case (case 4): (*a*) intermittency profile width, and (*b*) integrated intermittency length scale.

profiles are considered. The $\Delta r_{\mathrm{FWHM},\iota}/R_n$ values for case 4 have been plotted against axial location in figure 13(*a*). The points shown are the average of 18 values calculated from radial distributions of ι at negative-azimuthal angles between $\theta = 0°$ and $\theta = -170°$ (i.e. the bottom half of the mixing layer). In this way, interference from the injector strut evident in the upper portion of the mixing layer does not affect the results. The error bars shown are estimated from the intermittency uncertainty near $\iota = 0.5$. It is evident that the growth of the intermittent region is similar to that of the mixing-layer thickness in that this region grows faster for the swirling case than for the non-swirling case. Once again it appears that the increased growth rate associated with the swirling cases is observed only for $z/D_n > 6$. An alternative length scale is δ_ι:

$$\delta_\iota = \int_{r=0}^{r=\infty} \iota(r)\mathrm{d}r. \tag{7.2}$$

This parameter may be thought of as the characteristic dimension associated with fluid 'mixed' (or 'stirred') to the scale resolved by the camera (the camera's pixel size). This is in contrast to δ which represents the total extent of the mixing layer (encompassing both stirred and unstirred fluid). In a limited sense, δ_ι is a better mixing parameter than δ for combustion and other processes that require the fluids to be mixed at the molecular level. Although mixing at the molecular level remains to be demonstrated, knowing that fluid is stirred to the pixel level indicates those areas

where molecularly mixed fluid is likely to be found. Figure 13(*b*) reveals that, similar to $\Delta r_{\mathrm{FWHM},l}/R_n$, δ_l/R_n is greater for the swirling case than for the non-swirling case for $z/D_n > 6$. It can be concluded from figure 13 that not only is more entrainment taking place, but the amount of 'stirred' fluid is greater for case 4*b*.

The similarity between the three mixing-layer growth parameters δ, $\Delta r_{\mathrm{FWHM},l}/R_n$, and δ_l suggests that the growth of any of them, at least for the present case, may be used to characterize mixing-layer growth. This is important because it demonstrates that, in certain special cases, mean flow results are sufficient to characterize turbulence-driven phenomena.

8. Discussion of results

In the previous sections it was observed that the growth rates of swirling compressible mixing layers are greater than those of their non-swirling counterparts, and that the amount of this mixing enhancement scales with the degree of swirl. Furthermore, the analysis of instantaneous images reveals that the increased growth rates are accompanied by higher turbulence levels. Several related issues are discussed below.

An unexpected result of this study is that the mixing layers have an initial streamwise distance over which there is no apparent difference between the swirling mixing layer and its non-swirling counterpart. This may be due to the injector boundary layer, which may obscure any differences that do exist for $z/D_n \leqslant 6$. An alternative possibility is that the experimental techniques used here may not be sufficiently sensitive to discern any differences until they exceed a certain threshold. This suggestion is supported by the lack of any evidence of turbulence above that of the free stream for $z/D_n \leqslant 6$ in case 4 described earlier. One other possibility is that an 'inception' length may be required before the mechanism of mixing enhancement is activated.

Nonetheless, at a sufficient downstream distance, the turbulence levels associated with the swirling mixing layers are observed to be higher than those of the non-swirling cases. This result suggests that some mechanism associated with swirl is causing additional turbulence production, which causes more entrainment and a larger mixing-layer growth rate. Further discussion of the link between spreading rates and the degree of swirl is given in §9.

One issue that must be considered when comparing the swirling and non-swirling cases is the different turbulence levels at the nozzle exit. As discussed in §5, the swirling jets contained significant levels of turbulence near the axis that is presumably absent in the non-swirling cases. Although no firm conclusions can be drawn from the present measurements, it is likely that these increased turbulence levels play a role in the increased mixing observed. As previously noted, the high levels of turbulence observed in the swirling flows are most likely produced by a combination of sources including the swirl vanes' wake and the non-uniform tangential-velocity profile. Although the former source is linked to the means of swirl generation used here, swirling flows generated by other means also contain high core turbulence levels (i.e. Délery *et al.* 1984; Bandyopadhyay *et al.* 1991). Therefore, the turbulence found in the present swirling jets should not be considered peculiar to the swirl-generation means used here.

For the cases studied here, the degree of compressibility does not appear to significantly change the swirl-induced growth-rate enhancement. This implies that the effect of swirl may be beneficial over a large range of compressibility. This result may be important in hypersonic aircraft propulsion, where fuel injection in the supersonic flow in the combustion chamber would likely experience a range of

compressibility conditions over the flight envelope. On the negative side, swirling jets produce less thrust than their non-swirling counterparts. However, Dutton (1987) has demonstrated that the cause of this thrust reduction is reduced mass flow and not loss of specific impulse. Thus, application of this technique seems plausible, but its actual value in an operational system remains to be seen.

Finally, it became evident in the course of this study that no proper framework for analysing swirling compressible turbulent mixing layers exists. For instance, the concept of convective Mach number should at least be altered to account for the additional component of velocity present in a swirling jet. As a basis for such a framework, a plausible explanation for the mixing enhancement observed must be postulated.

9. Correlation parameter for growth-rate enhancement in compressible swirling mixing layers

Three primary views exist on the mechanism causing mixing enhancement in swirling jet flows. The first suggests that a fluid particle in the mixing layer of a swirling jet simply traverses a greater distance than that same particle would in the non-swirling case due to the additional azimuthal distance travelled. If the growth rate along this resultant helical path $\delta'_s = \mathrm{d}\delta/\mathrm{d}s$ equals the axial growth rate of the non-swirling jet $\delta'_z = \mathrm{d}\delta/\mathrm{d}z$, then the growth rate of the swirling jet, as observed in the axial direction, appears to be enhanced. Using these assumptions it can be shown that a moderately swirling jet (i.e. $\tau = 0.1$) experiences less than 2% swirl-induced mixing enhancement, far less than the experimentally observed values shown in figure 8. This indicates that the longer path length traversed by a particle in a swirling mixing layer may play a role in the mixing-enhancement observed, but it is not the primary mechanism.

The second view suggests that centrifugal instabilities are the cause of the observed enhancement (Panda & McLaughlin 1994; Mehta, Wood & Clausen 1991; Wu, Farokhi & Taghavi 1992; Cutler, Levey & Kraus 1995). Such instabilities arise in flows where the angular momentum decreases with increasing radius. The destabilizing effect of this mechanism is likely to be somewhat reduced in the present case because the density of the inner (primary) gas is lower than that of the outer (secondary) gas. Nonetheless, Cutler *et al.* (1995) have demonstrated that the enhanced mixing-layer growth rate caused by swirl correlates well with the Richardson number, a ratio of centrifugal forces to shearing forces. Although this result is promising, identifying the centrifugal instabilities by experimental or analytical means would support these findings.

The third explanation for the observed increased growth rates is that the addition of a tangential velocity to the flow creates an additional component of shear. This shear causes a significant component of streamwise vorticity ($\omega_{ml,z}$) in the mixing layer as shown in figure 14. This vorticity adds to the existing vorticity in the mixing layer, the azimuthal vorticity ($\omega_{ml,\theta}$), that is due to the axial-velocity difference. The total shear in the mixing layer has thus been increased causing additional turbulence production. More importantly, any mixing produced by the axial component of vorticity ($\omega_{ml,z}$) is not expected to be affected by compressibility (Morkovin 1992). The correlation parameter proposed here is based on this concept.

In a skewed mixing layer, the planar equivalent of the swirling jet, it has been shown that the mean flow may be separated into a uniform flow and a two-dimensional shear flow (Lu & Lele 1993). The uniform flow does not produce any shear, and

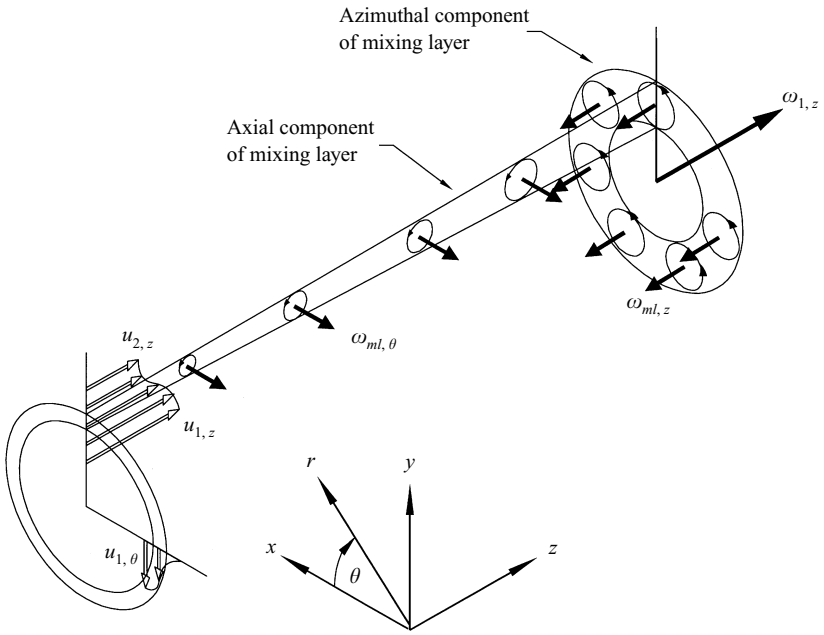

FIGURE 14. Schematic of a mixing layer surrounding a swirling jet showing velocity profiles, vorticity associated with the swirl ($\omega_{1,z}$), and vorticity components in the mixing layer ($\omega_{ml,z}, \omega_{ml,\theta}$). The swirling mixing layer has a streamwise-vorticity component not present in non-swirling jets.

thus the growth rate is uniquely determined by the two-dimensional shear flow. In two-dimensional incompressible mixing layers, the growth rates are proportional to the ratio of the velocity difference across the mixing layer, $\Delta u = u_1 - u_2$, to the convective velocity u_c (Papamoschou & Roshko 1988). As previously discussed, these incompressible growth rates are attenuated by compressibility. In the skewed mixing layer, Δu is that of the two-dimensional shear layer and u_c is replaced by the component of convective velocity in the growth direction. In such mixing layers, skewing increases the velocity ratio, which should enhance the mixing-layer growth rate, but it also increases compressibility, which should produce growth-rate attenuation effects. The results of linear stability analysis of these skewed mixing layers (Lu & Lele 1993) indicate that the predicted growth rates follow these trends. The overall result is that skewing the mixing layer enhances mixing, but less so as the convective Mach number increases.

In the swirling axisymmetric case, no such decomposition of the velocity field appears to exist due to the imposed symmetry. Despite this obstacle, several of the concepts discussed above appear to apply in this case also. As discussed, the mixing-layer growth rate of a non-swirling jet δ'_j is a function of the velocity difference, convective velocity, and an attenuation parameter that is a function of convective Mach number:

$$\delta'_j = f_1(u_{1,z} - u_{2,z}, M_{c,z}, u_{c,z}), \tag{9.1}$$

where the subscript z is added to denote the axial direction. Note that although the density ratio does not explicitly appear in (9.1), it appears in the convective velocity $u_{c,z}$ as shown in (1.2). The swirling-jet mixing-layer growth rate δ'_{sj} will have additional dependencies:

$$\delta'_{sj} = f_2(u_{1,z} - u_{2,z}, u_{1,\theta} - u_{2,\theta}, M_{c,z}, M_{c,\theta}, u_{c,z}). \tag{9.2}$$

The tangential component of the convective velocity $u_{c,\theta}$ has not been included in this functional relationship because axisymmetry requires that the jet grow only in the axial direction.

It has been shown that (9.1) has the following form (Papamoschou & Roshko 1988):

$$\delta'_j = K_z f(M_{c,z}) \frac{u_{1,z} - u_{2,z}}{u_{c,z}} = f(M_{c,z}) \delta'_i, \tag{9.3}$$

where K_z is a constant and an attenuation parameter $f(M_{c,z})$ has been added to account for the compressibility attenuation of growth rate. The dependency of $f(M_{c,z})$ on $M_{c,z}$ is shown in figure 7. Note that (9.3) is equivalent to (6.1) (with the exception of $f(M_{c,z})$) and is written in the present form to facilitate the arguments made here. For compressible swirling jets, it is proposed that the growth rate δ'_{sj} has an additional growth component due to the tangential-velocity difference:

$$\delta'_{sj} = g_1 \left(K_z f(M_{c,z}) \frac{u_{1,z} - u_{2,z}}{u_{c,z}}, K_\theta f(M_{c,\theta}) \frac{u_{1,\theta} - u_{2,\theta}}{u_{c,z}} \right), \tag{9.4}$$

where the exact functional form of g_1 is unspecified. The new terms K_θ and $f(M_{c,\theta})$ are the growth-rate constant and compressibility parameter, respectively, for the azimuthal term. Since (9.4) includes the sole parameter in (9.3), the ratio of δ'_{sj} and δ'_j can be written as a function of these same parameters or some combination of them such as their ratio:

$$\frac{\delta'_{sj}}{\delta'_j} = g_2 \left(\frac{K_\theta}{K_z} \frac{f(M_{c,\theta})}{f(M_{c,z})} \frac{u_{1,\theta} - u_{2,\theta}}{u_{1,z} - u_{2,z}} \right). \tag{9.5}$$

Note that the convective velocity $u_{c,z}$ cancels, and only the growth-rate constants, velocity differences across the mixing layer, and compressibility corrections are left. This equation may also be written in the following form:

$$\frac{\delta'_{sj}}{\delta'_j} = g_2(K\beta), \tag{9.6}$$

where $K = K_\theta / K_z$ and β incorporates the velocity difference ratio and the compressibility attenuation ratio. The left-hand side of (9.6) is identical to the ordinate of figure 8, and thus the measured enhancement may be plotted against the parameter β to determine the actual form of the relationship.

Although the velocities in (9.5) may be estimated using their values at $r = R_n$, determining the appropriate compressibility corrections is not straightforward. In order to determine these quantities, a convective Mach number appropriate to swirling flows must be defined. Lele & Lu (1993) and Cattafesta (as reported by Naughton & Settles 1994) have independently proposed definitions for the convective Mach number and convective velocity in mixing layers with more than one component of shear. Using arguments similar to that used for the development of (1.1*a*) and (1.1*b*), convective Mach numbers (now vectors) are suggested:

$$\boldsymbol{M}_{c,1} = (\boldsymbol{u}_1 - \boldsymbol{u}_c)/a_1, \tag{9.7a}$$

$$\boldsymbol{M}_{c,2} = (\boldsymbol{u}_c - \boldsymbol{u}_2)/a_2, \tag{9.7b}$$

which have the following components:

$$M_{c,1,z} = (u_{1,z} - u_{c,z})/a_1, \tag{9.8a}$$

$$M_{c,1,\theta} = (u_{1,\theta} - u_{c,\theta})/a_1, \tag{9.8b}$$

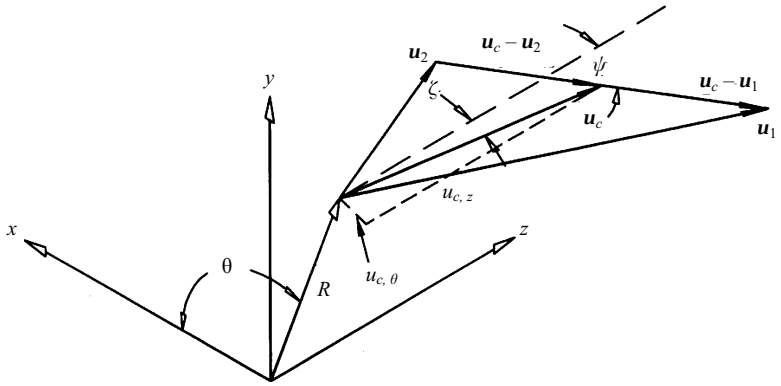

FIGURE 15. Schematic of the important parameters in the mixing layer surrounding a co-flowing jet in which both the primary flow and co-flow have tangential-velocity components. Vectors have been labelled as close to their end as possible for clarity.

$$M_{c,2,z} = (u_{c,z} - u_{2,z})/a_2, \tag{9.8c}$$

$$M_{c,2,\theta} = (u_{c,\theta} - u_{2,\theta})/a_2. \tag{9.8d}$$

The magnitudes of (9.7*a*) and (9.7*b*) are

$$M_{c,1} = ((u_{1,z} - u_{c,z})^2 + (u_{1,\theta} - u_{c,\theta})^2)^{1/2}/a_1, \tag{9.9a}$$

and

$$M_{c,2} = ((u_{c,z} - u_{2,z})^2 + (u_{c,\theta} - u_{2,\theta})^2)^{1/2}/a_2, \tag{9.9b}$$

respectively. Papamoschou & Roshko (1988) demonstrated that $M_{c,2}/M_{c,1} \approx (\gamma_1/\gamma_2)^{1/2}$ for $\gamma_1 \approx \gamma_2$, where γ is the ratio of specific heats. Using this argument and taking the ratio of (9.9*b*) to (9.9*a*) yield the following relationship:

$$\left(\frac{\gamma_1}{\gamma_2}\right)^{1/2} = \frac{a_1}{a_2}\frac{((u_{c,z} - u_{2,z})^2 + (u_{c,\theta} - u_{2,\theta})^2)^{1/2}}{((u_{1,z} - u_{c,z})^2 + (u_{1,\theta} - u_{c,\theta})^2)^{1/2}}. \tag{9.10}$$

By replacing a with $(\gamma p/\rho)^{1/2}$, where p is the static pressure, and assuming that $p_1 = p_2$ at the jet boundary, the following relationship may be determined:

$$\frac{(u_{c,z} - u_{2,z})^2 + (u_{c,\theta} - u_{2,\theta})^2}{(u_{1,z} - u_{c,z})^2 + (u_{1,\theta} - u_{c,\theta})^2} = \frac{\rho_1}{\rho_2}. \tag{9.11}$$

This equation, proposed in Naughton & Settles (1994), does not yield a unique solution for $u_{c,z}$ and $u_{c,\theta}$ since there is only one equation and two unknowns.

An additional restriction is required to solve (9.11) for the convective velocity components. In the planar skewed mixing layer, Lu & Lele (1993) have determined that, in most cases, the propagation angle of the most unstable waves (presumably travelling at the convective velocity) is the same as that of the effective shear direction. Since there is no analogous effective shear in the axisymmetric case, either a linear stability analysis must be performed or some other assumption must be made to determine the propagation angle. A reasonable assumption is that $\boldsymbol{u}_c$ lies somewhere between $\boldsymbol{u}_1$ and $\boldsymbol{u}_2$ as shown in figure 15. This condition requires that $\boldsymbol{u}_1 - \boldsymbol{u}_c$ and $\boldsymbol{u}_c - \boldsymbol{u}_2$ are both at an angle Ψ to the z-direction. A closer inspection yields a relationship between the components of $\boldsymbol{u}_1 - \boldsymbol{u}_2$, $\boldsymbol{u}_1 - \boldsymbol{u}_c$, and $\boldsymbol{u}_c - \boldsymbol{u}_2$:

$$\tan\Psi = \frac{u_{1,\theta} - u_{c,\theta}}{u_{1,z} - u_{c,z}} = \frac{u_{c,\theta} - u_{2,\theta}}{u_{c,z} - u_{2,z}} = \frac{u_{1,\theta} - u_{2,\theta}}{u_{1,z} - u_{2,z}}. \tag{9.12}$$

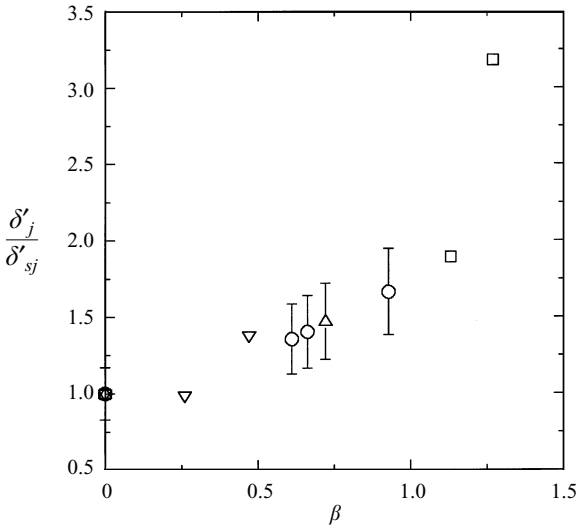

FIGURE 16. Mixing-layer growth-rate data plotted against a swirling mixing-layer growth-rate parameter β. Data from several studies are plotted: ○, case 1 of the present study, $M_{c,z} \approx 1.3$; △, case 4 of the present study, $M_{c,z} \approx 0.7$; □, Cutler *et al.* (1995), $M_{c,z} \approx 0.9$; and ▽, Mehta *et al.* (1992), $M_{c,z} \approx 0.0$.

These relationships can be used to eliminate either $u_{c,z}$ or $u_{c,\theta}$ from (9.11) to produce the following result for the convective velocity:

$$u_{c,z} = \frac{u_{1,z} + S^{1/2}u_{2,z}}{1 + S^{1/2}}, \tag{9.13a}$$

$$u_{c,\theta} = \frac{u_{1,\theta} + S^{1/2}u_{2,\theta}}{1 + S^{1/2}}, \tag{9.13b}$$

whose magnitude and direction are given by

$$u_c = \frac{[(u_{1,z} + S^{1/2}u_{2,z})^2 + (u_{1,\theta} + S^{1/2}u_{2,\theta})^2]^{1/2}}{1 + S^{1/2}}, \tag{9.14a}$$

and

$$\zeta = \arctan \frac{u_{1,\theta} + S^{1/2}u_{2,\theta}}{u_{1,z} + S^{1/2}u_{2,z}}. \tag{9.14b}$$

The relationships for u_c given by (9.13*a*) and (9.13*b*) are essentially identical to those given by Lu & Lele (1993) for skewed mixing layers.

Determining an expression for u_c allows the determination of the convective Mach number components given by (9.8). These values may then be used to evaluate the unknown compressibility attenuation parameters found in (9.5). Since the ratio K_θ/K_z is a constant, β represents an independent parameter against which the effect of swirl on mixing-layer growth rate may be evaluated. Cases 1 and 4 of the current study (the only cases with LDV measurements) are shown in figure 16 plotted versus β. In addition, data from other swirling-jet studies (Cutler *et al.* 1995 and Mehta *et al.* 1991) are also plotted. These data cover a range of compressibility, and thus they should provide a useful test of the correlation parameter proposed here.

Several features of this figure are worth noting. First, the data appear to collapse to a single curve when plotted against β. Second, for low-β values typical of

incompressible swirling jets and low-swirl compressible jets, the effect of swirl on mixing appears to be negligible. Third, for β-values above 0.3, the mixing-layer growth-rate enhancement increases steadily with β. Fourth, the highest β-point from the study by Cutler *et al.* (1995) appears to deviate significantly from the trend indicated by the other points on the graph. Cutler *et al.* (1995) suggest that this latter result may have been due to vortex breakdown, which would cause additional turbulence production and mixing. This suggests that the parameter β correlates the data up to some maximum level beyond which other factors not considered in determining β become important. Nonetheless, the data shown here appear to confirm that β serves as a useful parameter for estimating mixing enhancement over a large range of swirl.

These results raise an interesting question. Why does mixing enhancement increase with β? In the incompressible case, the tangential velocity difference $(u_{1,\theta} - u_{2,\theta})$ is responsible for any enhancement since both $f(M_{c,\theta})$ and $f(M_{c,z})$ are unity. However, as axial compressibility increases, the value of $f(M_{c,z})$ drops, increasing β and, as shown in figure 16, the swirl enhancement. This latter effect is a direct result of the proposed independence of tangential mixing mechanisms from axial compressibility. It is important to note that, while mixing enhancement increases with increasing $M_{c,z}$ (for given values of R and S), the absolute mixing-layer growth rate (the measured growth rate before being normalized) still falls with increasing $M_{c,z}$.

Although the arguments presented here conclusively demonstrate that swirl enhances mixing, it is important to understand the limitations of this analysis. For example, the tangential velocity of the primary stream along the mixing interface is estimated using a curve fit to data taken near the maximum $u_{1,\theta}$, point. Errors in the estimated strength parameter k_t of 10% can shift the data points laterally in figure 16 by as much as 0.125, while errors in r_t have little effect. Using a predicted value at $r = R_n$ for the tangential velocity $u_{1,\theta}$ is also suspect at locations downstream. This is due to the mixing layer growth, which causes the inside edge of the mixing layer to move radially inward where $u_{1,\theta}$ is higher. For the present swirling flows, this could possibly cause greater enhancement at downstream locations due to the potentially greater tangential velocity difference there.

In spite of these limitations, it appears that β correlates, at least to first order, the existing swirl-enhanced mixing data, thereby capturing the key elements involved. Similar to the effect of skewing planar mixing layers, the addition of swirl to the round jet increases mixing-layer growth rate. Furthermore, for a given tangential velocity difference, the swirl enhancement of mixing-layer growth rate increases as axial compressibility (represented here by $M_{c,z}$) increases. Owing to its dependence on quantities (the velocity ratio and compressibility of the jet) that represent these two effects, β is an appropriate parameter to characterize the swirl enhancement of mixing-layer growth rates in swirling jets.

10. Concluding remarks

Several interesting results have arisen from this study, the most important of which is that swirl enhancement of compressible turbulent mixing has been conclusively demonstrated. The data of this study indicate that this enhancement occurs over a wide range of compressibility, and is manifested by a change in the turbulent structure of the mixing layer. A parameter β that correlates the swirl-induced growth-rate enhancement for mixing layers surrounding compressible swirling jets has also been determined. This parameter indicates that compressibility plays a role in determining

the exact amount of mixing enhancement, a result that is not obvious from the experimental data of this study alone. It is also interesting that the amount of swirl required to achieve a significant mixing enhancement is relatively small, suggesting that the streamwise component of vorticity caused by swirl has an important effect on the mixing process. This is in agreement with the hypothesis that, in contrast to their azimuthal counterparts, the mixing caused by the streamwise components of vorticity in the mixing layer is relatively unaffected by axial compressibility.

Despite the current results, many questions remain unresolved. The parameter β proposed here appears to indicate the important quantities that determine swirl-induced mixing enhancement, but the basis for its development still must be proven conclusively. This and other remaining questions will only be answered with further experimental and computational research whose goal is to ascertain the vortical turbulent structure present in swirling compressible jets. Typical turbulence measurements (single-point statistics) alone will not be sufficient for this purpose. Rather, some two-point measurements, preferably time-resolved, will be necessary to achieve this goal (a non-trivial task in the environment of the compressible jet). Additional insight into the mechanisms causing swirl-enhanced mixing can be provided by linear stability theory. In addition to lending support to the swirl mixing-enhancement parameter developed here, such an analysis can suggest the swirl characteristics (velocity profile, strength, etc.) that produce the maximum amplification rates in the mixing layer.

Nonetheless, this study has provided a solid basis upon which further investigation of swirl enhancement may be built. For instance, a practical direction of work would be to optimize the swirl profile for enhancement. Since this enhancement is dependent upon the tangential velocity difference across the mixing layer, adding swirl only to the mixing layer could provide more effective enhancement than the current approach. Another area that should be studied is the investigation of alternative methods of creating the streamwise vortical structures (responsible for the enhanced growth rates) found in swirling mixing layers.

This work was supported in part by NASA Grant NAG-1-872 monitored by Dr G. B. Northam. The first author was also supported by NASA Grant NGT-50400. We thank our colleagues at the Penn State Gas Dynamics Lab for their assistance with this experiment. We also thank Andrew Cutler, Brian Levey, and Donna Kraus for providing us with the details of their swirling jet study. Finally, we would like to extend our appreciation to the reviewers for their constructive comments on this work.

Appendix A. Swirl number estimation

Owing to the high cost of helium, the nozzle-exit profiles for several of the cases in table 1 were not measured. Since there is no direct way to evaluate a swirl number τ_n for these cases, a method of generalizing the amount of swirl produced by a given set of vanes is needed, regardless of the injectant gas and nozzle used. The swirl is quantified using a swirl number $\tau = H_z/(F_z R_n)$, which is the ratio of angular momentum flux to axial momentum flux at a given axial location. Since, to first order, the vanes impart a tangential velocity that is only dependent on the incoming axial velocity, the swirl number at their exit should be independent of both the injected gas and nozzle. Therefore, a means of estimating the swirl number at the vane exit τ_v for those cases where nozzle-exit velocity profiles exist has been developed. The average

of the calculated values for τ_v for a given set of vanes is then used to estimate the swirl number at the nozzle exit τ_n given the nozzle and gas used.

The procedure is as follows. First, the tangential-velocity data at the nozzle exit for a given case are fit using (5.1), thereby determining k_t and r_t. Second, estimated values of the density and axial velocity at the nozzle exit (ρ_n and $u_{z,n}$) are predicted using one-dimensional isentropic theory and the stagnation conditions known in the plenum chamber of the injector. These values are assumed to be constants, independent of radius. Third, (5.3) is integrated to evaluate the swirl number at the nozzle exit τ_n. Fourth, values for the density and axial velocity at the vane exit (ρ_v and $u_{z,v}$) are estimated in the same way as ρ_n and $u_{z,n}$. Fifth, the value of $F_z = 2\pi \int_0^R \rho u_z^2 r \mathrm{d}r$ at the vane exit ($F_{z,v}$) is calculated. Finally, by assuming that H_z is conserved through the nozzle (i.e. $H_{z,v} = H_{z,n}$), the swirl number at the exit of the swirl vanes $\tau_v = H_{z,v}/(F_{z,v}R_v)$ is approximated.

The estimated values of τ_v are approximately constant for each set of vanes as expected. The scatter in the τ_v-values is greatest for the 30°-vanes, with typical standard deviations being 15% of the mean. Therefore, the averages of these τ_v-values for each set of vanes ($\bar{\tau}_v$) are assumed to be sufficiently accurate to estimate a swirl number at the nozzle exit ($\tilde{\tau}_n$).

The estimated value of τ_n ($\tilde{\tau}_n$) is calculated as follows. First, the value of ($\bar{\tau}_v$) corresponding to the vanes used for the case of interest is selected. Second, the angular momentum flux is calculated using $H_{z,v} = \bar{\tau}_v F_{z,v} R_v$. Finally, by again assuming H_z remains unchanged through the nozzle, the swirl number at the nozzle exit is calculated using $\tilde{\tau}_n = H_{z,v}/(F_{z,n}R_n)$.

The accuracy of the estimated swirl number $\tilde{\tau}_n$ calculated using the above method is estimated by comparing its value to that determined directly from the measured velocity profiles. The average error of the 12 cases is 16% of the value of τ_n.

Appendix B. PLS image analysis

In this Appendix, the determination of mixing-layer thickness and turbulence information from PLS images, such as those in figures 3(*a*) and 3(*b*), will be presented. Since a detailed description of these analysis techniques is given by Naughton (1993), only a brief overview is presented here.

In order to determine the mixing-layer concentration thickness δ_c from the raw PLS images, the following steps were followed. First, the image intensity $I(r, \theta, z)$ at each point along a radial cut taken from the geometric centre of the jet was normalized between zero (in the centre) and unity (in the free stream) producing the normalized-intensity distribution I^*. This step was performed in order to account for the variations in laser sheet intensity, seeding density, and pulse-to-pulse laser intensity. This normalization procedure is strictly valid only if the imaging camera has a linear response to light intensity, which was determined to be the case for the range of illumination used with both cameras here. Second, the locations in the radial cut of normalized intensity I^* defining the mixing-layer thickness, 0.3 and 0.7 in this study, were determined. Repeating this process for 60 such radial cuts (6° intervals) yielded an inner and outer boundary of the mixing region. To determine a characteristic mixing-layer thickness, the radii of equivalent circles with the same areas as those contained within the inner and outer boundaries were calculated. The difference between these radii was taken as the mixing-layer concentration thickness δ_c.

As are all definitions of mixing-layer thickness, the definition of δ_c based upon the 0.3 and 0.7 normalized-intensity boundaries is somewhat arbitrary . However, the differences between different mixing-layer thickness definitions may be accounted for by proper non-dimensionalization or by the appropriate conversion factor. In other words, all such mixing-layer thickness definitions are related to one another. The present values were chosen to minimize the error associated with the data analysis procedure described above.

As opposed to the mixing-layer thickness, which may be calculated from a single image (instantaneous or time-averaged), the intermittency and r.m.s. intensities require an ensemble of instantaneous images. To calculate the intermittency at a given point, intensity values along a radial cut of one instantaneous image were again normalized between zero and unity. This step was repeated for the same radial cut in each successive image of the ensemble. Next, two normalized-intensity values were chosen ($I_l^* = 0.25$ and $I_h^* = 0.75$ for the present study) and the intermittency value along the radial cut was determined using

$$\iota = \mathrm{P}(I_l^* < I^*(r, \theta, z) < I_h^*), \tag{B 1}$$

where P is the probability of the relation inside the parentheses. Once again, the normalized-intensity values chosen as the upper and lower thresholds for determining the intermittency are arbitrary. However, since they are used solely for the purpose of comparing the intermittent regions of different jets, the exact values are unimportant so long as they are consistent.

In contrast to calculating the intermittency only along sample radial slices, $\bar{I}$ (mean intensity) and σ_I (r.m.s. intensity) were calculated at each spatial location in the image using the intensities of the corresponding point in each instantaneous raw image in the ensemble. This analysis produced two resultant images, one representative of the mean intensity values and the other corresponding to the fluctuating intensities. The mean intensities thus produced were then normalized along a radial cut to produce a normalized mean intensity distribution $\bar{I}^*$ that varied between zero in the centre of the primary stream to unity in the secondary stream. Each r.m.s. intensity value $\sigma_I(r)$ along the cut was then divided by the value of $\bar{I}(r)$ at the same location, and subsequently multiplied by the corresponding $\bar{I}^*$-value to produce σ_I^*. The normalized r.m.s. intensity value σ_I^* should not be confused with a turbulence intensity quantity (i.e. $\sigma_I(r)/\bar{I}(r)$) but may be thought of as the fluctuation of that point scaled with respect to the unmixed secondary mean value $\bar{I}(r \to \infty)$.

REFERENCES

Bandyopadhyay, P. R., Stead, D. J. & Ash, R. L. 1991 Organized nature of a turbulent trailing vortex. *AIAA J.* **29**, 1627–1633.

Bogdanoff, D. W. 1983 Compressibility effects in turbulent shear layers. *AIAA J.* **21**, 926–927.

Bonnet, J. P. & Chaput, E. 1986 Large-scale structures visualization in a high Reynolds number, turbulent flat-plate wake at supersonic speed. *Exps. Fluids* **4**, 350–356.

Bowker, A. H. & Liebermann, G. J. 1972 *Engineering Statistics*. Prentice-Hall.

Bradshaw, P. 1966 The effect of initial conditions on the development of a free shear layer. *J. Fluid Mech.* **26**, 225–236.

Brown, G. L. & Roshko, A. R. 1974 On density effects and large structure in turbulent mixing layers. *J. Fluid Mech.* **64**, 775–781.

Cattafesta, L. N. 1992 Experiments on shock/vortex interaction. PhD thesis, Pennsylvania State University.

Chao, Y. C., Han, J. M. & Jeng, M. S. 1990 A quantitative laser sheet image processing method for the study of the coherent structure of a circular jet flow. *Exps. Fluids* **9**, 323–332.

Chevray, R. 1968 The turbulent wake of a body of revolution. *Trans. ASME* D: *J. Basic Engng* **90**, 275–284.

Clemens, N. T. & Mungal, M. G. 1992 Two- and three-dimensional effects in the supersonic mixing layer. *AIAA J.* **30**, 973–982.

Coles, D. 1985 Dryden Lecture: The uses of coherent structure. *AIAA Paper* 85-0506.

Cutler, A. D., Levey, B. S. & Kraus, D. K. 1993 An experimental investigation of supersonic swirling jets. *AIAA Paper* 93-2922.

Cutler, A. D., Levey, B. S. & Kraus, D. K. 1995 On the near-field flow of supersonic swirling jets. *AIAA J.* **33**, 876–881.

Délery, J., Horowitz, E., Leutcher, O. & Solignac, J. L. 1984 Fundamental studies on vortex flows. *Recherche Aerospatiale* **2**, 1–24.

Dimotakis, P. E. 1991 Turbulent free shear layer mixing and combustion. In *High Speed Flight Propulsion Systems* (ed. S. Murthy & E. Curran). Progress in Aeronautics, vol. 137, pp. 265–340. AIAA.

Dutton, J. C. 1987 Swirling supersonic nozzle flow. *J. Prop.* **3**, 342–349.

Elliot, G. & Samimy, M. 1990 Compressibility effects in free shear layers. *AIAA Paper* 90-0705.

Farokhi, S., Taghavi, R. & Rice, E. J. 1989 Effect of initial swirl distribution on the evolution of a turbulent jet. *AIAA J.* **27**, 700–906.

Fourgette, D. C., Mungal M. G. & Dibble, R. W. 1991 Time evolution of the shear layer of a supersonic axisymmetric jet. *AIAA J.* **29**, 1123–1130.

Goebel, S. G. & Dutton, J. C. 1991 Experimental study of compressible turbulent mixing layers. *AIAA J.* **29**, 538–946.

Gruber, M. R., Messersmith, N. L. & Dutton, J. C. 1992 Three-dimensional velocity measurements in a turbulent compressible mixing layer. *AIAA Paper* 92-3544.

Hartnett, J. P. & Eckert, E. R. G. 1957 Experimental study of the velocity and temperature distribution in a high velocity vortex-type flow. *Trans. ASME* **79**, 751–758.

Hilsch, R. 1947 The use of the expansion gases in a centrifugal field as cooling process. *Rev. Sci. Instrum.* **18**, 108 – 113.

Jackson, T. L. & Grosch, C. E. 1989 Inviscid spatial stability of a compressible mixing layer. *J. Fluid Mech.* **208**, 609–637.

Khorrami, M. R. 1995 Stability of a compressible axisymmetric swirling jet. *AIAA J.* **33**, 650–658.

Lele, S. K. 1989 Direct numerical simulation of compressible free shear flows. *AIAA Paper* 89-0374.

Lele, S.K. 1994 Compressibility effects on turbulence. *Ann. Rev. Fluid Mech.* **26**, 211–254.

Lessen, M., Singh, P. J. & Paillet, F. 1974 The stability of a trailing line vortex. Part 1. Inviscid theory. *J. Fluid Mech.* **63**, 753–763.

Lu, G. & Lele, S. K. 1993 Inviscid instability of a skewed compressible mixing layer. *J. Fluid Mech.* **249**, 441–463.

Mandella, M. & Bershader, D. 1987 Quantitative study of the compressible vortex: generation, structure, and interaction with airfoils. *AIAA Paper* 87-0328.

Maurice, M. S. 1992 Laser velocimetry seed particles within compressible, vortical flows. *AIAA J.* **30**, 376–383.

McGregor, I. 1961 The vapour-screen method of flow visualization. *J. Fluid Mech.* **11**, 481–511.

Mehta, R. D., Wood, D. H. & Clausen, P. D. 1991 Some effects of swirl on turbulent mixing layer development. *Phys. Fluids* A **3**, 2717–2724.

Messersmith, N. L., Dutton, J. C. & Krier, H. 1991 Experimental investigation of large scale structures in compressible mixing layers. *AIAA Paper* 91-0244.

Metwally, O., Settles, G. & Horstman, C. 1989 Experimental study of shock wave/vortex interaction. *AIAA Paper* 89-0082.

Morkovin, M. V. 1992 Mach number effects on free and wall turbulent structures in light of instability flow interactions. In *Studies In Turbulence* (ed. T. B. Gatski, S. Sarkar & C. G. Speziale), pp. 269–284. Springer.

Morris, P. J., Giridharan, M. G. & Lilley, G. M. 1990 Turbulent mixing in plane and axisymmetric shear layers. *Proc. R. Soc. Lond.* A **431**, 219–243.

NAUGHTON, J. W. 1993 The enhancement of compressible turbulent mixing via streamwise vorticity. PhD thesis, Pennsylvania State University.

NAUGHTON, J., CATTAFESTA, L. & SETTLES, G. 1989 Experimental study of the effect of streamwise vorticity on supersonic mixing enhancement. *AIAA Paper* 89-2456.

NAUGHTON, J. W., CATTAFESTA, L. N. III & SETTLES, G. S. 1993*a* Miniature, fast-response five-hole conical probe for supersonic flowfield measurements. *AIAA J.* **31**, 453–458.

NAUGHTON, J. W., CATTAFESTA, L. N. & SETTLES, G. S. 1993*b* Experiments on the enhancement of compressible mixing via streamwise vorticity, Part II - Vortex strength assessment and seed particle dynamics *AIAA Paper* 93-0742.

NAUGHTON, J. W. & SETTLES, G. S. 1994 A theoretical framework for mixing layers surrounding compressible turbulent swirling jets. *AIAA Paper* 94-2245.

PANDA, J. & MCLAUGHLIN, D. K. 1994 Experiments on the instabilities of a swirling jet. *Phys. Fluids* **6**, 263–276.

PAPAMOSCHOU, D. 1990 Communication paths in the compressible shear layer. *AIAA Paper* 90-0155.

PAPAMOSCHOU, D. & ROSHKO, A. R. 1988 The compressible turbulent shear layer: an experimental study. *J. Fluid Mech.* **197**, 453–477.

POVINELLI, L. A. & EHLERS, R. C. 1972 Swirling base injection for supersonic combustion ramjets. *AIAA J.* **10**, 1243–1244.

PRASAD, R. R. & SREENIVASAN, K. R. 1990 Three-dimensional imaging and the structure of passive scalar fields in fully turbulent flows. *J. Fluid Mech.* **216**, 1–34.

SAMIMY, M. & LELE, S. K. 1991 Motion of particles with inertia in a compressible free shear layer. *Phys. Fluids* A **3**, 1915–1923.

SANDHAM, N. & REYNOLDS, W. 1990 The compressible mixing layer: linear theory and direct simulation. *AIAA Paper* 90-0371.

SCHETZ, J. A. & SWANSON, R. C. 1973 Turbulent jet mixing at high supersonic speeds. *Z. Flugwiss.* **21**, 166–173.

SCHNEIDERMAN, A. M. & SUTTON, G. W. 1970 Measurements of turbulent mixing statistics in the near wake of a supersonic cone. *Phys. Fluids* **13**, 1679–1682.

SWITHENBANK, J. & CHIGIER, N. A. 1969 Vortex mixing for supersonic combustion. In *XIIth Intl Symp. on Comb.,* pp. 1152–1162. The Combustion Institute.

WEGENER, P. P., & STEIN, G. D. 1969 Light-scattering experiments and theory of homogeneous nucleation in condensing supersonic flow. In *XIIth Intl Symp. on Comb*., pp. 1183–1191. The Combustion Institute.

WILCOX, D. C. 1993 *Turbulence Modeling for CFD*. DCW Industries.

WU, C., FAROKHI, S. & TAGHAVI, R. 1992 Spatial instability of a swirling jet - theory and experiment. *AIAA J.* **30**, 1545–1552.